Contract Report
Reservoir Characterization Research Laboratory
Carbonate Reservoirs

Waterflood Performance Analysis for the South Cowden Grayburg Reservoir, Ector County, Texas

James W. Jennings, Jr.

Funding by

Amoco, Aramco, ARCO, BP International, Exxon, Fina, JNOC, Marathon, Oxy, Pennzoil, Petroleum Development Oman, Phillips, Shell Canada, Shell Western, Texaco, TOTAL, Unocal, and the U.S. Department of Energy

Additional support from

Geomath, Landmark, OGCI Software, and Terra Science

Bureau of Economic Geology
Noel Tyler, Director
The University of Texas at Austin
Austin, Texas 78713-8924

October 1996

Contents

Figures

Tables

Waterflood Performance Analysis for the South Cowden Grayburg Reservoir

Abstract

A reservoir engineering study was conducted of waterflood performance in the South Cowden field, an Upper Permian Grayburg reservoir on the Central Basin Platform in West Texas. The study was undertaken to understand the historically poor waterflood performance, evaluate three techniques for incorporating petrophysical measurements and geological interpretation into heterogeneous reservoir models, and identify issues in heterogeneity modeling and fluid-flow scaleup that require further research. The approach included analysis of relative permeability data, analysis of injection and production data, heterogeneity modeling, and waterflood simulation.

The poor South Cowden waterflood recovery is due, in part, to completion of wells in only the top half of the formation. Recompletion of wells through the entire formation is estimated to improve recovery in ten years by 6 percent of the original oil in place in some areas of the field.

A direct three-dimensional stochastic approach to heterogeneity modeling produced the best fit to waterflood performance and injectivity, but a more conventional model based on smooth mapping of layer-averaged properties was almost as good. The results reaffirm the importance of large-scale heterogeneities in waterflood modeling but demonstrate only a slight advantage for stochastic modeling at this scale.

All the flow simulations required a reduction to the measured whole-core k_v/k_h to explain waterflood behavior, suggesting the presence of barriers to vertical flow not explicitly accounted for in any of the heterogeneity models. They also required modifications to the measured steady-state relative permeabilities, suggesting the importance of small-scale heterogeneities and scaleup. Vertical flow barriers, small-scale heterogeneity modeling, and

relative permeability scaleup require additional research for waterflood performance prediction in reservoirs like South Cowden.

Introduction

The South Cowden field is located in West Texas, Ector County, just outside the city of Odessa (fig. 1). It is a shallow-water carbonate reservoir on the eastern edge of the Central Basin Platform, in the Upper Permian Grayburg Formation directly above the San Andres (Ruppel and Bebout, 1996). The Grayburg outcrops in the Guadalupe Mountains, where ongoing studies provide geological insight, geometrical measurements, and petrophysical data

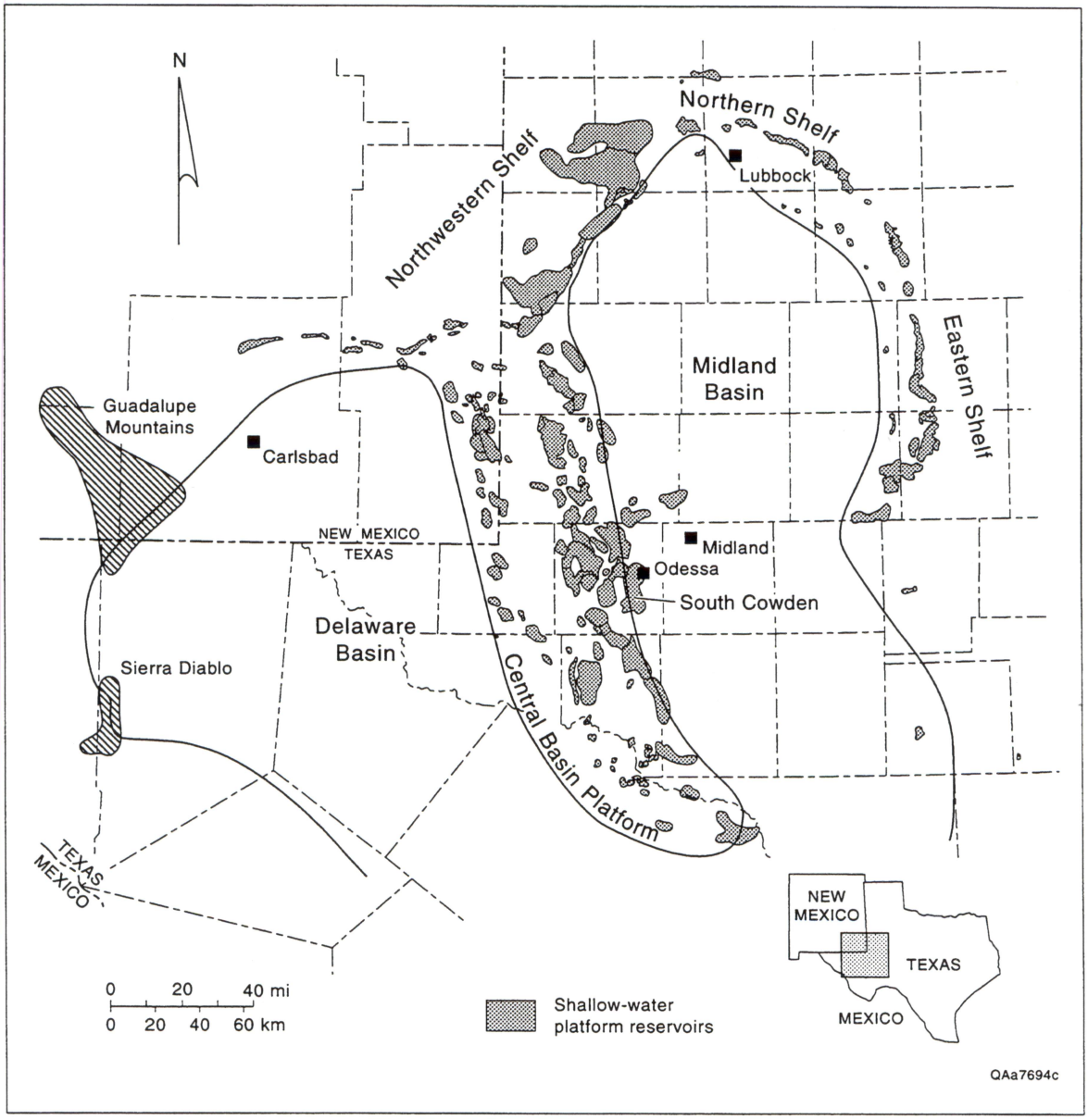

Figure 1. Shallow-water carbonate platform reservoirs of West Texas and New Mexico, including those producing from the Grayburg Formation. From Ruppel and Bebout, 1996.

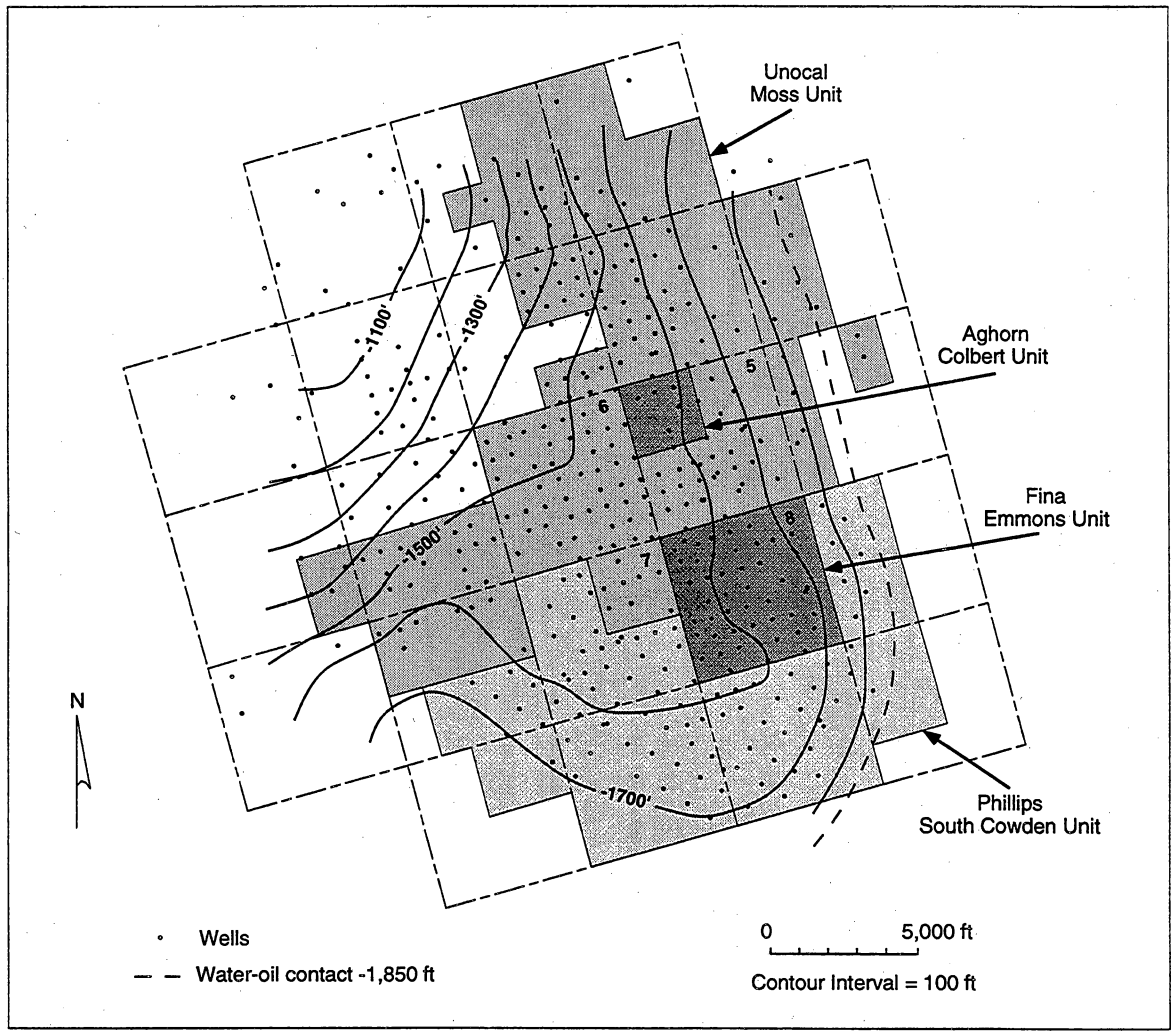

Figure 2. Unit boundaries and structure on top of the Grayburg Formation in the South Cowden field. Modified from Ruppel and Bebout, 1996.

useful in construction of subsurface reservoir models (Kerans and Nance, 1991; Barnaby and Ward, 1995).

The field was discovered in 1933 (Young and Vaughn, 1957); oil production began in 1948, and waterflooding in 1962. Sufficient data for production and injection analysis were provided for the period 1965–1993 in the Colbert (Aghorn operator), Emmons (Fina operator), Moss (Unocal operator), and South Cowden (Phillips operator) units (fig. 2). Thus, the South Cowden field, with thirty years of waterflood history, provides a good opportunity to test the impact of various reservoir-modeling methods on waterflood performance prediction. Recovery efficiency in the field is disappointing, even less than

the typically low recoveries in other West Texas shallow-water carbonate reservoirs (30 percent of the initial oil in place) (Kerans and others, 1994). Thirty years of waterflood in the South Cowden field has recovered only 21 percent of the original oil in place in sections 5–8, 45 percent of the estimated displaceable oil.

This report describes a South Cowden reservoir engineering study that had the following objectives:

(1) Understand the reasons for the poor waterflood performance and make recommendations to improve it.

(2) Test three methods of modeling heterogeneity for waterflood simulation: smooth interpolation of properties vertically averaged within high-frequency cycles, stochastic simulation of the same vertically averaged properties, and direct three-dimensional stochastic simulation of the foot-by-foot well-log data.

(3) Evaluate the heterogeneity modeling methods by comparison of waterflood simulation results with field performance. Determine whether the modeled heterogeneities can account for the poor waterflood performance.

(4) Identify issues in heterogeneity modeling and fluid-flow scaleup that require further research for better performance predictions in carbonate reservoirs.

The study is described in the next five sections of this report. First, the modeling of relative permeability and residual oil saturation is explained. The residual oil saturation models were required for analysis of production and injection data, which is described in the second section. Third and fourth are heterogeneity modeling and waterflood simulation. In the fifth section the additional recovery that may be obtained by deepening the wells through the entire formation is estimated. The report ends with conclusions and recommendations for additional research.

Relative Permeability Modeling

The displacement of oil by water in porous materials is influenced by many factors, including the geometry of the pore space, the interfacial tension, the wettability of the rock-fluid system, and the saturation history (Amyx and others, 1960). These effects are usually accounted for in flow models through relative permeability (k_r) and capillary pressure (p_c) saturation functions empirically determined from small samples of the rock-fluid system. Capillary pressure quantifies the difference between phase pressures at a given average saturation due to the tension and configuration of fluid-fluid interfaces in the pore space; it is important in modeling the initial equilibrium saturation distribution in a reservoir. Relative permeability quantifies the ease with which different fluid phases flow at a given saturation. The k_r saturation functions usually have a dominant effect on waterflood performance predictions and must be modeled carefully for the fluid-flow calculations to accurately represent subsurface fluid movement.

Relative permeability measurements and models

Carefully measured k_r data are available from two cored wells in the South Cowden field. The data include water-oil k_r measurements for eight core plugs. Four were measured with the steady-state method and the other four with the unsteady-state method (fig. 3). The steady-state method is a direct measurement of k_r obtained by controlling separately the flow rate of each phase and observing the resulting pressure drops and average saturations when a stabilized condition is reached (Collins, 1990). The unsteady-state method is an indirect measurement that uses Buckley-Leverett and Welge theory to calculate the k_r implied by the production and pressure history observed in a laboratory waterflood (Collins, 1990). This method is a waterflood performance prediction in reverse, but with certain simplifying assumptions (one-dimensional flow, homogeneous rock properties, negligible capillary and gravity effects); rather than using k_r to calculate waterflood

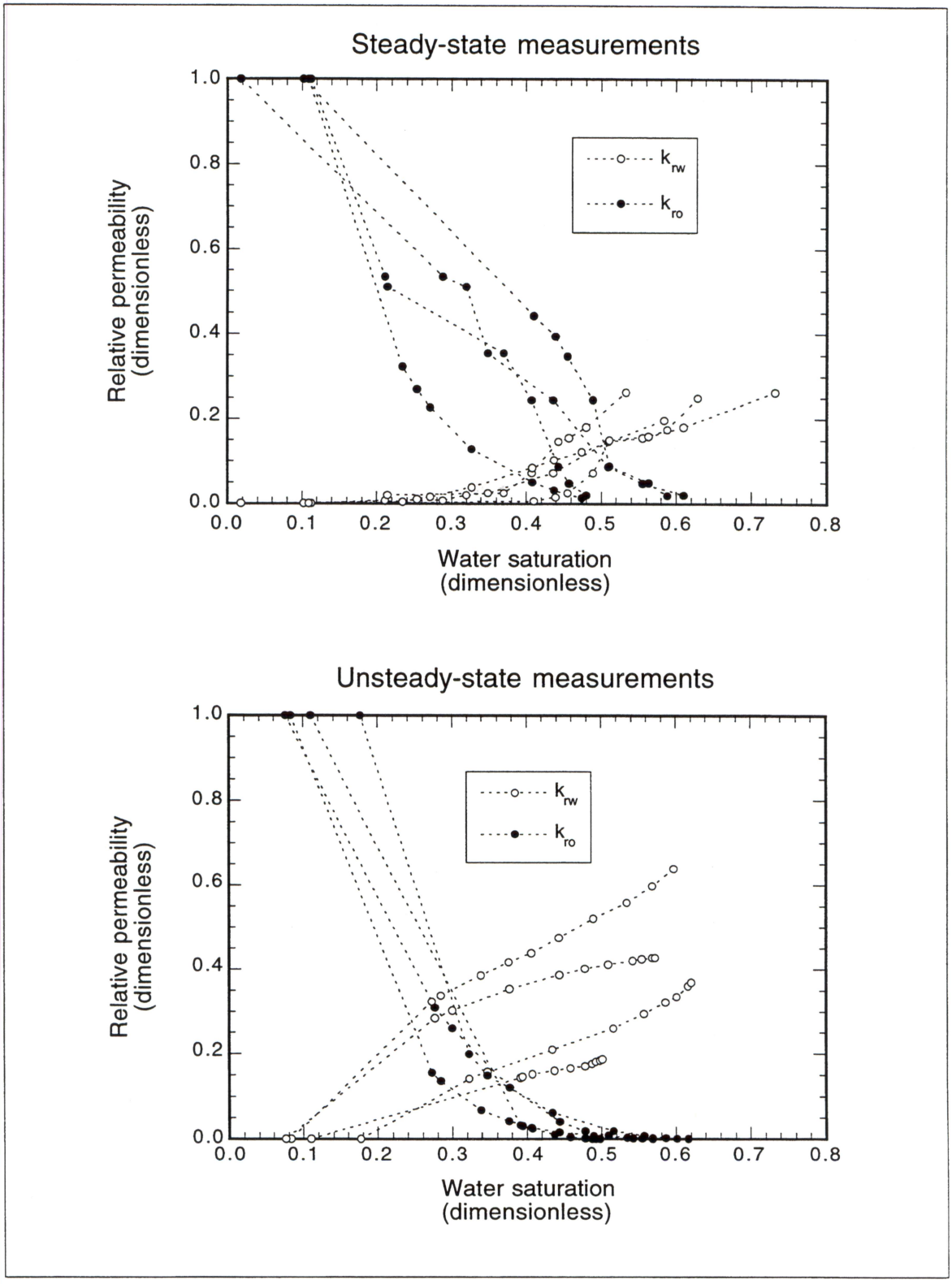

Figure 3. Steady-state and unsteady-state k_r measurements, relative to oil permeability at initial water saturation, water saturation increasing.

behavior, observed waterflood behavior is used to calculate k_r. Both methods are generally conducted at flow velocities much higher than in the subsurface to avoid capillary effects. The unsteady-state method is the faster of the two, but it is more adversely affected by heterogeneities within a core sample.

The scatter in the South Cowden k_r data is substantial, but it does not necessarily imply measurement errors and could be due entirely to property variations between the samples. Unfortunately, there are insufficient samples to conduct a meaningful statistical analysis of the variability. Therefore, approximate models were constructed to represent a simple average of the data. First, the k_r data for each core sample were modeled with power laws of the form

$$k_{rw}(s_w) = k^*_{rw}\left(\frac{s_w - s_{w-}}{s_{w+} - s_{w-}}\right)^{e_w} \tag{1}$$

and

$$k_{ro}(s_w) = \left(\frac{s_{w+} - s_w}{s_{w+} - s_{w-}}\right)^{e_o} \tag{2}$$

where k_{rw} and k_{ro} are the water and oil relative permeabilities, s_w is the water saturation, s_{w-} and s_{w+} are the left and right endpoint water saturations, e_w and e_o are exponents controlling the k_r curve shapes, and k^*_{rw} is the water endpoint relative permeability. In these models k_{rw} and k_{ro} are zero at s_{w-} and s_{w+} respectively. The k_r's are expressed relative to the oil permeability at initial water saturation; thus, the k_{ro} endpoint is one. The fitted parameters s_{w-}, s_{w+}, e_w, e_o, and k^*_{rw} for each sample were averaged to give steady-state and unsteady-state k_r models (fig. 4).

A systematic difference between the steady-state and unsteady-state measurements is apparent. Unsteady-state k_r models will predict less effective displacement of oil by water; at any given water saturation the unsteady-state k_{ro} is smaller and the unsteady-state k_{rw} is larger than the corresponding

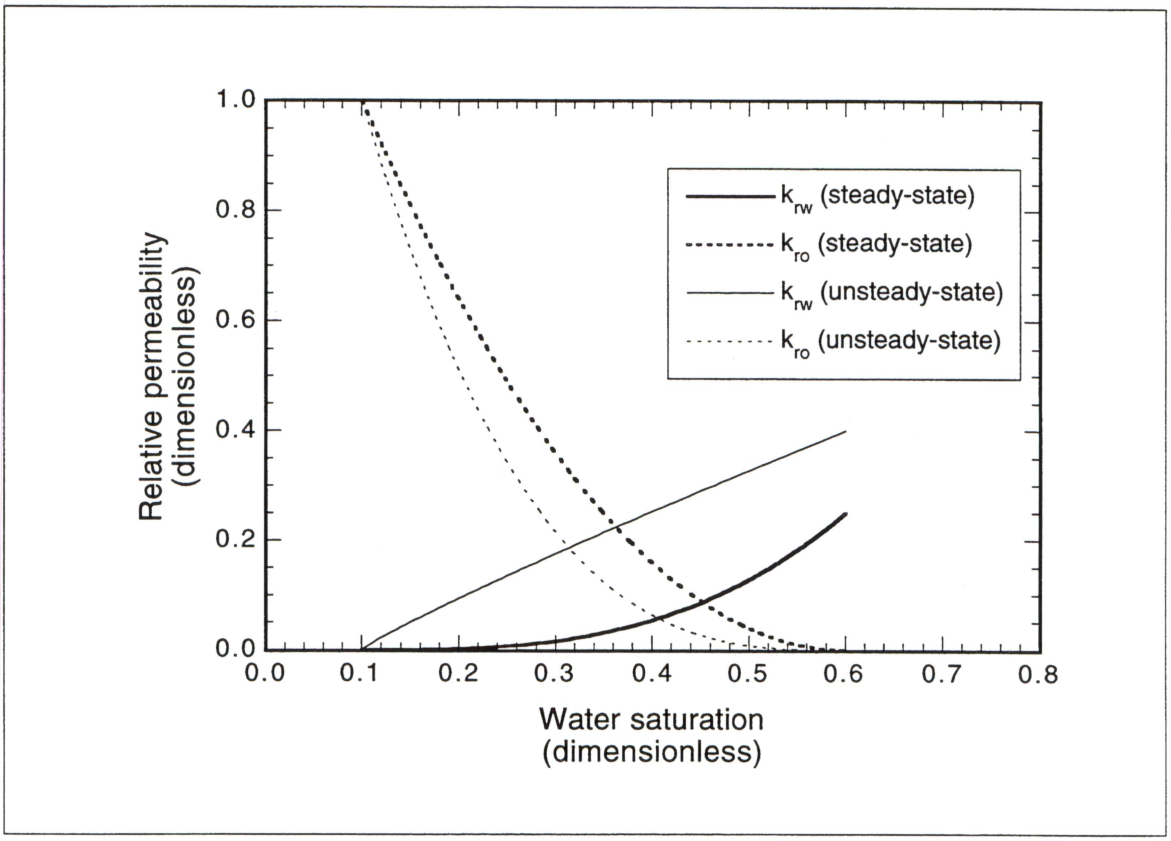

Figure 4. Steady-state and unsteady-state k_r models, relative to oil permeability at initial water saturation, water saturation increasing

steady-state k_r's. The most likely explanation for the difference is the influence of heterogeneity within a core sample on the unsteady-state test. Water tends to flow in the higher permeability paths, giving a larger apparent k_{rw}, and bypassed oil is left to flow in the lower permeability regions, giving a smaller apparent k_{ro}. The steady-state method is less affected by core-sample heterogeneity because measurements are made only after steady-state is reached and water has displaced more oil from lower permeability portions of the sample.

The steady-state and unsteady-state measurements were conducted with two different sets of core samples, but the differences do not explain the k_r discrepancy. The two sets are not *systematically* different on the basis of either porosity-permeability or endpoint saturations (fig. 5). Likewise, texture differences do not explain the k_r discrepancy; there are class 1 and class 2 fabrics in each set (Lucia, 1995; F.J. Lucia, personal communication, 1996).

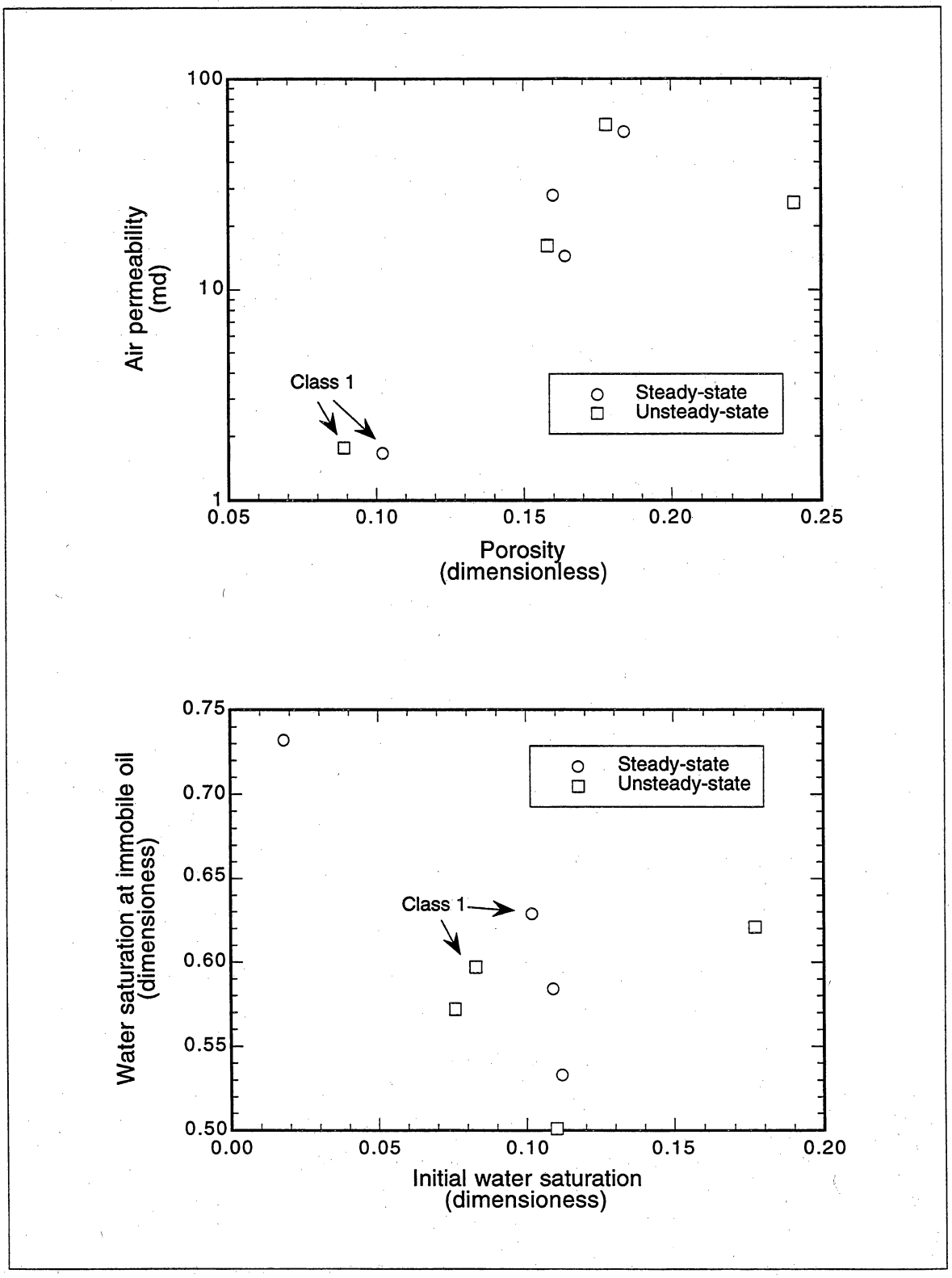

Figure 5. Porosity and air permeability (top), and endpoint water saturations (bottom) for the eight core samples used in k_r measurement. Samples with class 1 textural classification are indicated, all others are class 2.

Experimental procedures were similar for the eight experiments up to the point of water-oil displacement. The most important difference is that the unsteady-state experiments were conducted with recombined live crude oil, but the steady-state experiments used dead crude diluted with iododecane to match reservoir viscosity. The different fluids may have had some effect on the wettability of the samples; the unsteady-state experiments may have been less water wet and closer to the subsurface wettability state. However, the wettability effect is probably too small to explain the k_r discrepancy (G.A. Pope, personal communication, 1996). In all other respects the experiments were conducted to represent the reservoir wettability as much as possible. Wettability effects may explain part of the k_r difference, but most of it is probably due to heterogeneity.

Choosing k_r models for flow simulation

There are many heterogeneities in the subsurface that affect oil displacement by water. In principle, the accepted way to account for this is through numerical flow simulation with grid properties to represent heterogeneities larger than the grid blocks, and scaleup to represent those smaller than the grid blocks. Steady-state k_r models are probably a better representation of flow in the reservoir at the core-plug scale. Thus, these models should be used as a starting point in scaleup from the core-sample scale to "effective" k_r models at the grid-block scale. The result is similar to the effect of heterogeneity on unsteady-state k_r tests; the water tends to flow in the higher permeability paths, giving a larger apparent k_{rw}, and the bypassed oil is left to flow in the lower permeability regions, giving a smaller apparent k_{ro}.

Both unsteady-state k_r and grid-block effective k_r will predict less efficient waterfloods than steady-state k_r models. However, there is no guarantee that unsteady-state k_r is a good approximation of effective k_r because the heterogeneities are at very different scales and the flow is at a very different velocity.

Unfortunately, there are no generally accepted methods or widely available tools for relative permeability scaleup; it is currently a topic of active research.

Construction of tools and comparison of methods for k_r scaleup were beyond the scope of this study, so the waterflood simulations summarized later in this report used the simple steady-state and unsteady-state k_r models described above. The steady-state models give an optimistic estimate of waterflood performance, and the unsteady-state models at least show the direction things would change with proper scaleup.

Initial-residual oil saturation models

The eight k_r measurements all had similar initial oil saturations (s_{oi}, average about 90 percent) and residual oil saturations (s_{or}, average about 40 percent) (fig. 6). The eight samples were apparently selected with a bias toward higher s_{oi}. The average s_{oi} for the South Cowden reservoir is much smaller (about 46 percent from well-log estimates above the water-oil contact in sections 5–8). The subsurface s_{oi}'s are frequently much smaller than 90 or even 40 percent, and they are variable. Thus, the flow models constructed in this study utilized variable initial saturations derived from well-log models described later in this report in a section on heterogeneity modeling.

Likewise, it makes no sense to build a flow model with a uniform s_{or} of 40 percent because there are places with less than 40 percent oil initially. Thus, s_{or} should also be variable and should depend upon s_{oi}. Usually, s_{or} is an increasing function of s_{oi}. If s_{oi} is zero, s_{or} is zero, and the more oil there is to start with, the higher the residual will be. Unfortunately, the South Cowden k_r data do not cover a wide enough range of s_{oi} to define the s_{oi}-s_{or} relationship; it was necessary to assume some models (fig. 6).

The "worst case" model assumes that all oil up to 40 percent initial saturation is immobile, and only oil above that saturation can be displaced with water. The "optimistic" model assumes that a fixed fraction (4/9) of any initial oil saturation is immobile. The "average" model is just the arithmetic average of the other two. All three models reproduce the average s_{oi} and s_{or} from the eight k_r experiments. The average model was used for most simulations; the other two were used less often to test sensitivities. Realistic s_{oi}-s_{or} relationships

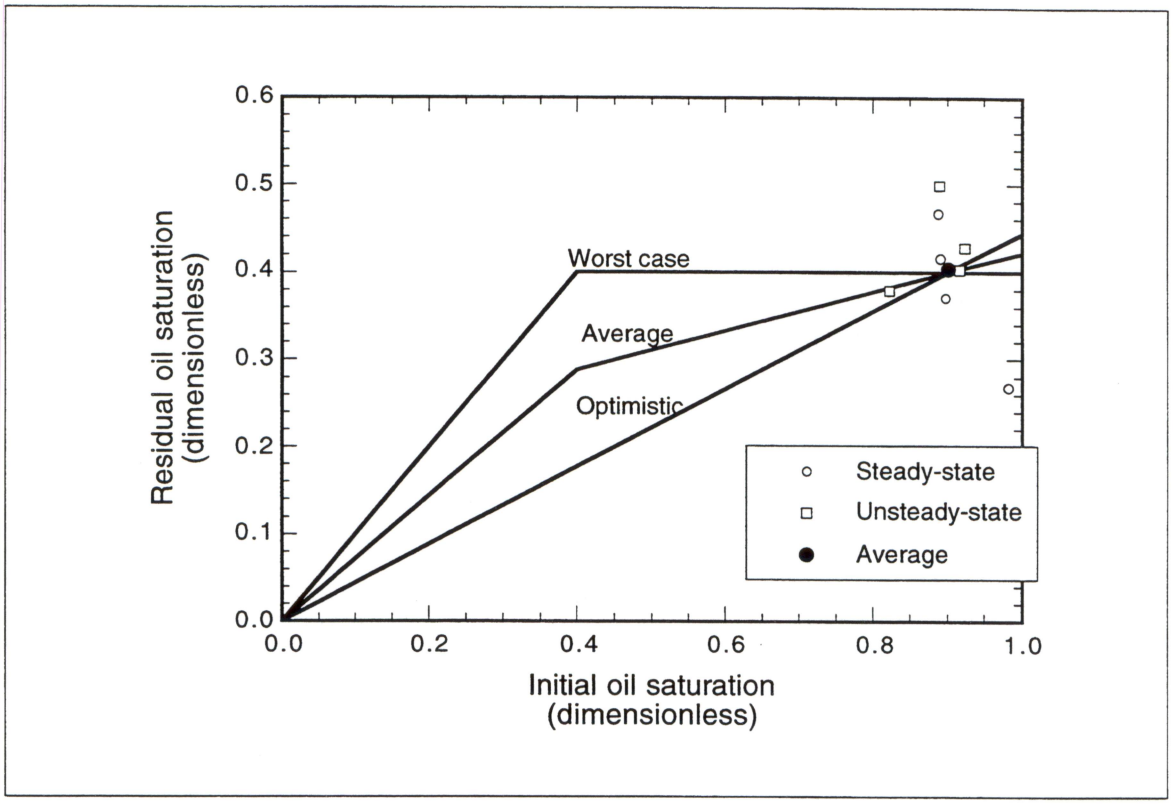

Figure 6. Initial-residual oil saturation models used to set residual saturations and for k_r endpoint scaling.

are probably smooth curves, unlike the worst-case and average models, which have sharp bends at 40 percent. However, the models shown here were adequate for the purposes of this study and were convenient when calculating displaceable hydrocarbon pore volume.

The effect of variable s_{oi} and s_{or} on relative permeability was modeled with "k_r endpoint scaling"; the k_r endpoint saturations are allowed to vary among the grid blocks, but the k_r curve *shapes* are the same, normalized to the local endpoints. There are two approximations implied by this use of k_r endpoint scaling. First, the initial saturation is assumed to be the same as the immobile-water saturation. This is probably a valid assumption above the capillary transition zone and is supported by the observation of low water-production rates early in the field history. Second, the k_r curve shapes are approximated as constants throughout the reservoir. This approximation is probably *not* accurate, but there is insufficient k_r data to define a model of variable k_r curve shapes.

Production and Injection History

The ability to explain a reservoir's production history does not guarantee the accuracy of future predictions, but without it there can be little confidence in any model's reliability. Thus, comparison of model calculations with production data is an important step in any reservoir study. Unfortunately, a reservoir's performance can be a complicated response to many interacting factors; the challenge is to focus upon parts of the problem that have a direct bearing on the objectives of the study, while performing comparisons in a way that avoids distraction from other issues. The goals in analysis of South Cowden production data were to understand the primary flow mechanisms, select a few characteristics that are diagnostic of reservoir heterogeneity, and prepare the data for meaningful comparison with flow models.

Pressure data and fluid properties

South Cowden pressure data are incomplete, but it appears that the average pressure dropped significantly from the initial 1,760 psi at -1,600 ft subsea, to less than 400 psi just before waterflood startup (Suter and others, 1961; Unocal, 1962). The pressure began climbing immediately with water injection. The average reservoir pressure is probably much higher than 400 psi now, but the local pressure varies significantly from place to place; 1991 estimates of producing bottom-hole pressure in the Moss Unit range from several hundred to about 2,000 psi, while two injectors had sand-face pressures approaching 3,000 psi (S. Landon, personal communication, 1995). Fortunately, the bubble-point pressure (325 psi) and natural gas content (160 scf/stb) of South Cowden crude is quite low and any free gas movement was probably limited to isolated areas. Thus, a reasonable approximation for analysis of production data and modeling of fluid movement is that only two phases are present in the subsurface: oil and water.

The original oil volume factor was close to one (1.078 rb/stb) (Suter and others, 1961) due to the low gas content. It has probably not changed much with time, despite the large pressure variations, because the reservoir has

been above its bubble point nearly everywhere. Therefore, incompressible flow is probably a good approximation. It is also convenient, eliminating analysis and modeling of historical pressure change as a goal of the study. The following production and injection analysis was conducted using fluid volumes converted to subsurface conditions with constant volume factors. The water volume factor was estimated from a published correlation (1.01 rb/stb) (Craft and others, 1991).

Injection and production balance

Although pre-1965 production estimates are available for the entire field (e.g., Young and Vaughn, 1957) this study has used only data collected since that time, when records for individual wells became sufficiently complete in the study area. A graph of cumulative total fluid production against cumulative injection is useful in summarizing waterflood injection balance; the slope of the plot will be one if injection is exactly replacing produced fluids, independent of any unknown production prior to waterflood. Injection volumes for the entire field averaged 21 percent greater than production from 1965 through 1993 (fig. 7). This overinjection was not constant through time; it was greater at the beginning of waterflood and has decreased significantly to a well-balanced condition in the 1990s. It's not likely that pressure changes over time are enough to account for the extra injection volume. Hence, there may have been some loss of injection fluid to other formations.

A similar analysis was performed for sections 5, 6, 7, and 8 in the central part of the field, counting $^1/_2$ the volume for edge wells and $^1/_4$ for corner wells (fig. 8). Section 5 was underinjected early in the waterflood and overinjected later, for a net balance of fluid volumes. Section 8 was also underinjected early in the waterflood. Later, the section 8 injection and production rates were nearly in balance, but the early underinjection was never replaced. Sections 6 and 7 were overinjected, but the balance was improved later for section 6.

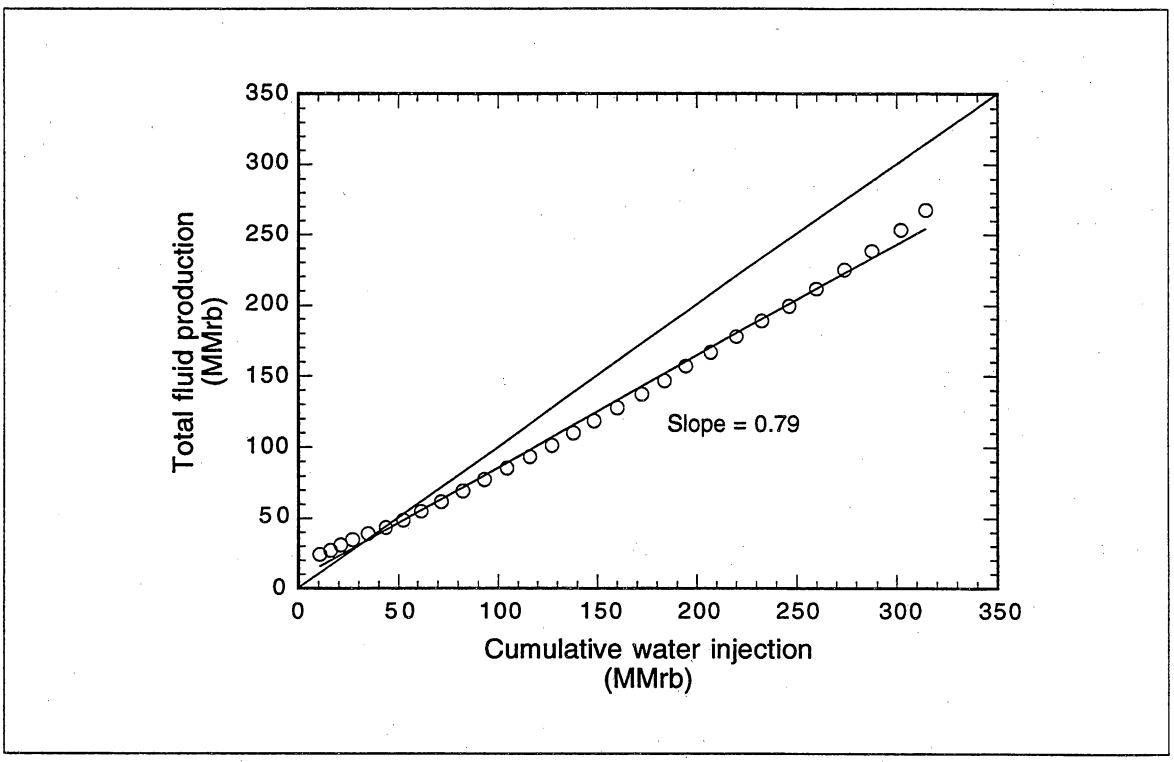

Figure 7. Cumulative total fluid production and water injection corrected to subsurface conditions for the South Cowden field, 1965–1993.

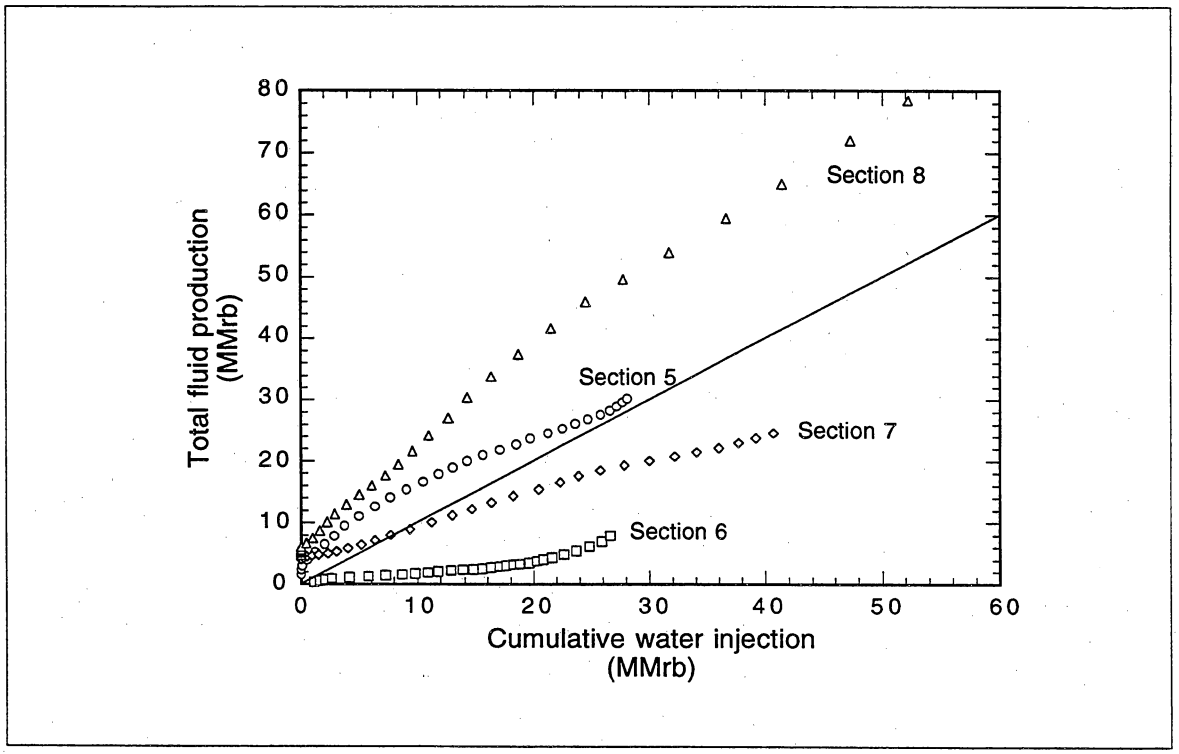

Figure 8. Cumulative total fluid production and water injection corrected to subsurface conditions for sections 5–8, 1965–1993.

The lack of balance between injection and production volumes for 640-acre areas of the field indicates that there may have been significant regional movement of fluids. Detailed and specific history-matching studies of small areas considered in isolation could be misleading; models of large portions of the field would probably be required for detailed history matching. A history-matching exercise of this magnitude is beyond the scope of the study; only general comparisons between field and model were attempted.

Waterflood displacement performance

Of course, it is important to understand not just the total fluid production, but how much of it is *oil*. Oil production is frequently summarized with a graph of the cumulative recovery as a function of time, but the injection rate influences the timing of oil production and is not constant. Instead, it is helpful to graph cumulative waterflood oil production as a function of the cumulative injection. This device allows the waterflood displacement performance to be considered separately from the well injectivity and productivity. It also allows the displacement performance to be compared with laboratory experiments that occur at a much smaller time scale.

An additional consideration when comparing field and laboratory waterfloods is the different initial water saturations. The average for sections 5–8 was 54 percent (from volumetric calculations using well-log data), but the average for the eight core samples described previously was much less, about 10 percent. However, the waterflood performance can be compared on an equivalent basis by using injection and production volumes expressed as a fraction of the *displaceable hydrocarbon pore volume* (DHCPV), the part of the pore volume between the two relative-permeability endpoints. The DHCPVs for each section were estimated by including the s_{oi}-s_{or} models in the volumetric calculations.

Some of the recorded water injection, instead of contributing to oil displacement from the Grayburg, may have been lost to other formations. The possibility of regional fluid movement also means that water injection in

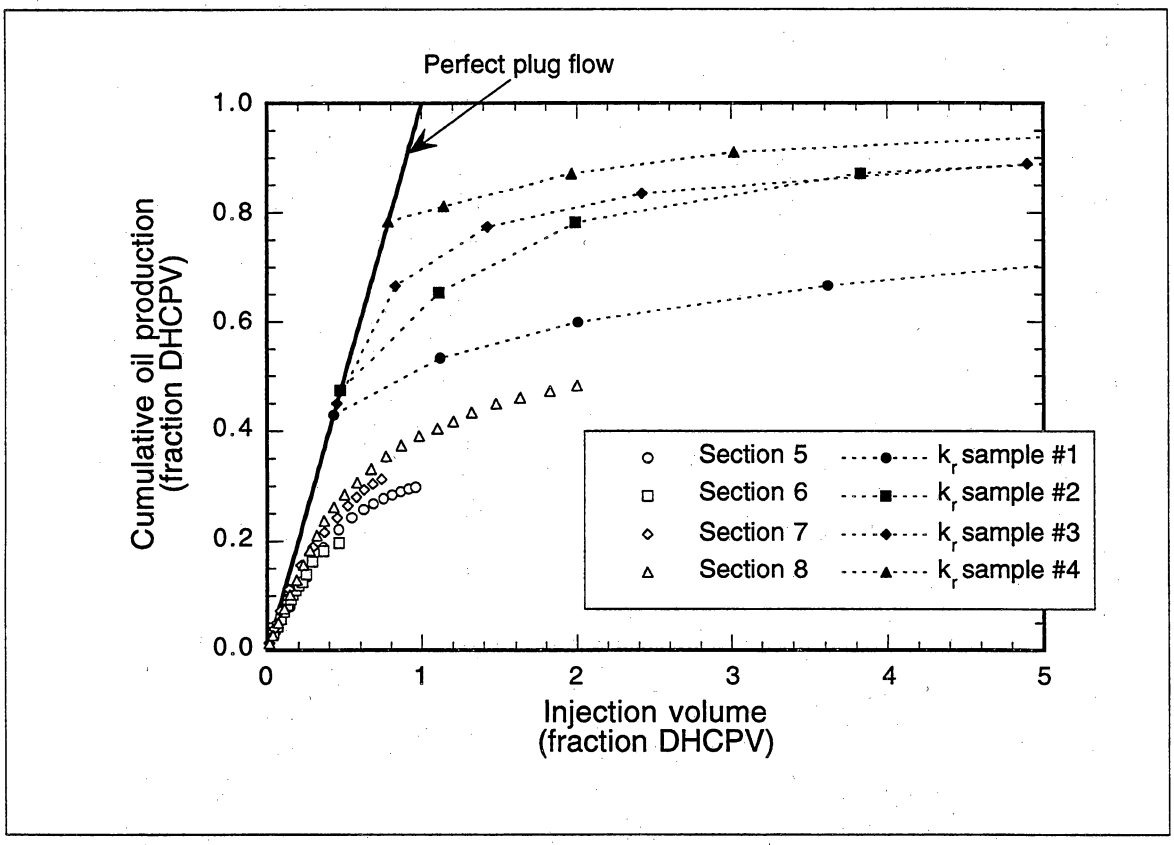

Figure 9. Waterflood displacement performance for sections 5–8 compared with four laboratory waterfloods on small samples. The field DHCPV's were computed with the average residual saturation model. An idealized displacement with perfect plug flow is also shown.

one area may contribute to oil production in another. Thus, it is important to estimate the *net* water volume entering an area: injected water, plus water migrating in from other areas, minus water migrating out. A convenient way to do this, consistent with the approximation of incompressible flow, is to assume that the net water injection is equal to the total fluid production after the start of waterflood; any over- or underinjection is assumed to have gone to, or come from, somewhere else. Of course, this procedure assumes that all the fluid migrating between regions is water, whereas some of it could be oil, but the only way to do better than this is to conduct a full-field simulation study.

These ideas were used to compare the waterflood performance in sections 5–8 with the four laboratory experiments used in unsteady-state relative permeability measurement (fig. 9). It is immediately apparent that the

reservoir has performed much worse on the average than the laboratory waterfloods. A major objective of this study is to understand the important mechanisms responsible for this behavior and the degree of heterogeneity required to reproduce it in a flow model. To reach this objective, it is sufficient to match waterflood performance within the observed range; detailed prediction of any particular area is not necessary.

After the basic flow mechanisms of the reservoir are understood, it will be possible to address effectively the reasons for the significant variability in waterflood performance observed in different areas of the field (fig. 9). Understanding the differences in behavior across the field would require more detailed modeling and was not an objective of this study. Nevertheless, it is worthwhile to mention some of the factors that may combine to produce the observed effects:

1. Fluid movement across section boundaries—Sections 5 and 6 performed worse than 7 and 8, perhaps because some of the water injected in sections 5 and 6 displaced oil that was eventually produced elsewhere. Perhaps some of the water produced from sections 5 and 6 was not injected there but migrated from somewhere else.

2. Different heterogeneity patterns—Sections 5 and 6 had earlier water breakthrough and higher water cuts, perhaps because the reservoir there behaves more layer-like with more laterally connected high-permeability pathways and stronger vertical flow barriers. There is a difference in diagenetic patterns across the field that may be responsible for part of the observed behavior (Ruppel and Bebout, 1996), but on the basis of this factor alone one might have expected the poorer performing sections to be 6 and 7, not 5 and 6.

3. Different positions on structure—Sections 5 and 8 are lower on structure, with more pore volume below the water-oil contact, than 6 and 7. The lower-quality rock tends to be in the bottom of the formation; thus, sections 5 and 8 have a larger fraction of their hydrocarbon pore volume

in better rock. However, like the diagenetic patterns, this effect alone does not explain the behavior, because poorer performance is expected from sections 6 and 7, not 5 and 6.

4. Different relative permeability characteristics—Sections 5 and 6 may simply be characterized by less favorable relative permeabilities. However, this speculation is impossible to evaluate without additional k_r measurements across the field.

5. Different waterflood management practices—The spacing of wells, injection patterns, completion strategies, and timing of water injection all vary across the field. Any of these factors can lead to differences in waterflood performance.

Another way to compare laboratory and field performance is to use Buckley-Leverett predictions from the k_r models, rather than the laboratory displacements themselves. This approach makes comparison with the other four steady-state experiments possible; for these measurements there was no comparable waterflood displacement. It also effectively summarizes the four unsteady-state displacements (fig. 10). The logarithmic time scale allows visualization of projected long-term behavior.

Both of the Buckley-Leverett waterflood predictions overestimate recovery, largely because all large-scale heterogeneity and sweep effects have been omitted. The unsteady-state k_r models come closer to the field performance, but this is a consequence of core-scale heterogeneity and unrealistically large laboratory flow rates. An ideal flow model for the South Cowden reservoir would include the effects of heterogeneity at all scales, either explicitly, or implicitly through scaleup, and would give a good match to the field performance starting from the *steady-state* relative permeabilities. The difference between the steady-state Buckley-Leverett prediction and the observed behavior is a measure of the effects that must be accounted for through characterization and modeling of heterogeneity.

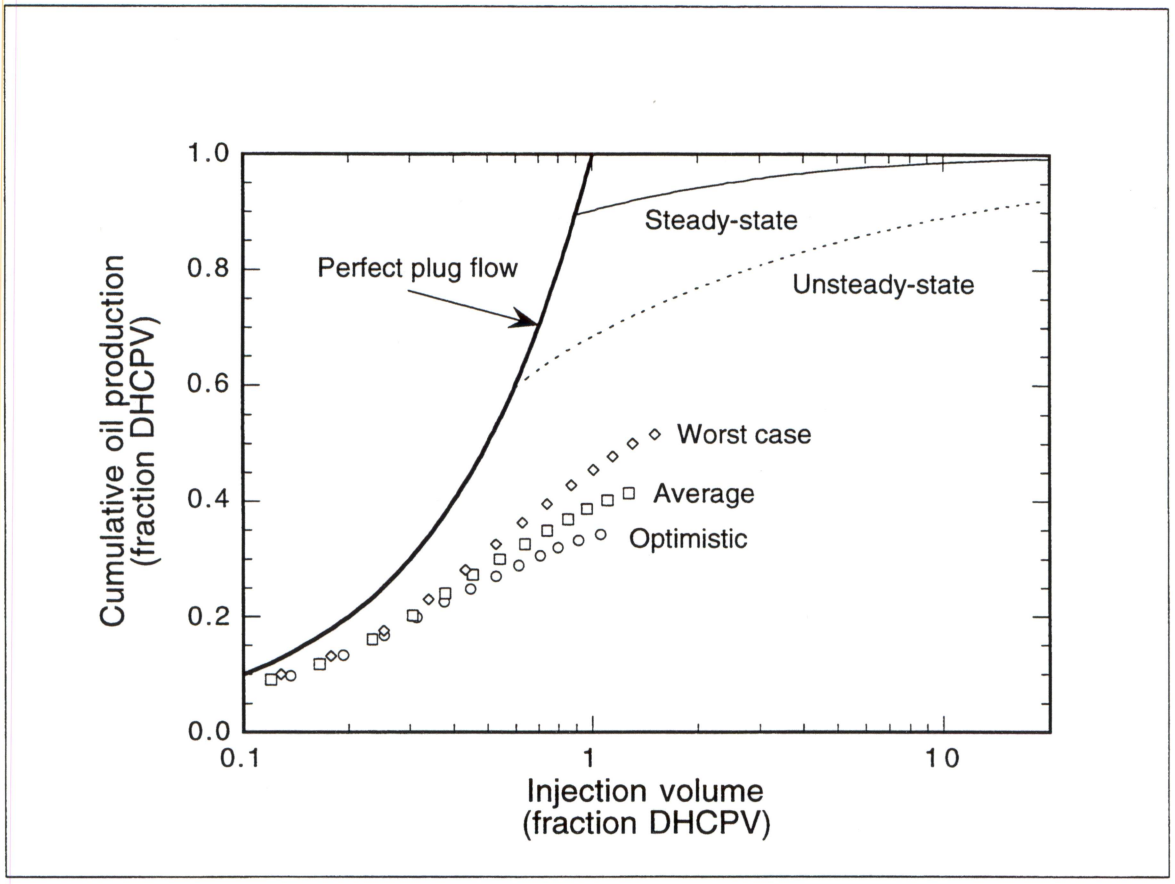

Figure 10. Total waterflood displacement performance for sections 5–8, using the three residual saturation models (symbols), compared with Buckley-Leverett predictions from the two relative permeability models (curves).

An important source of uncertainty in comparisons of field performance and model projections is the s_{oi}-s_{or} model. This uncertainty is illustrated in fig. 10 by showing the total performance for sections 5–8 converted to a DHCPV basis using each of the three s_{oi}-s_{or} models.

Injectivity, injection patterns, and well completions

Injectivity is a parameter of economic importance in waterfloods because it affects the timing and rate of oil displacement. In the South Cowden field, there is enough water-injection history to reasonably measure injectivity. In many other situations without sufficient waterflood history, it is necessary to *predict* the injectivity from models of the rock properties and heterogeneity.

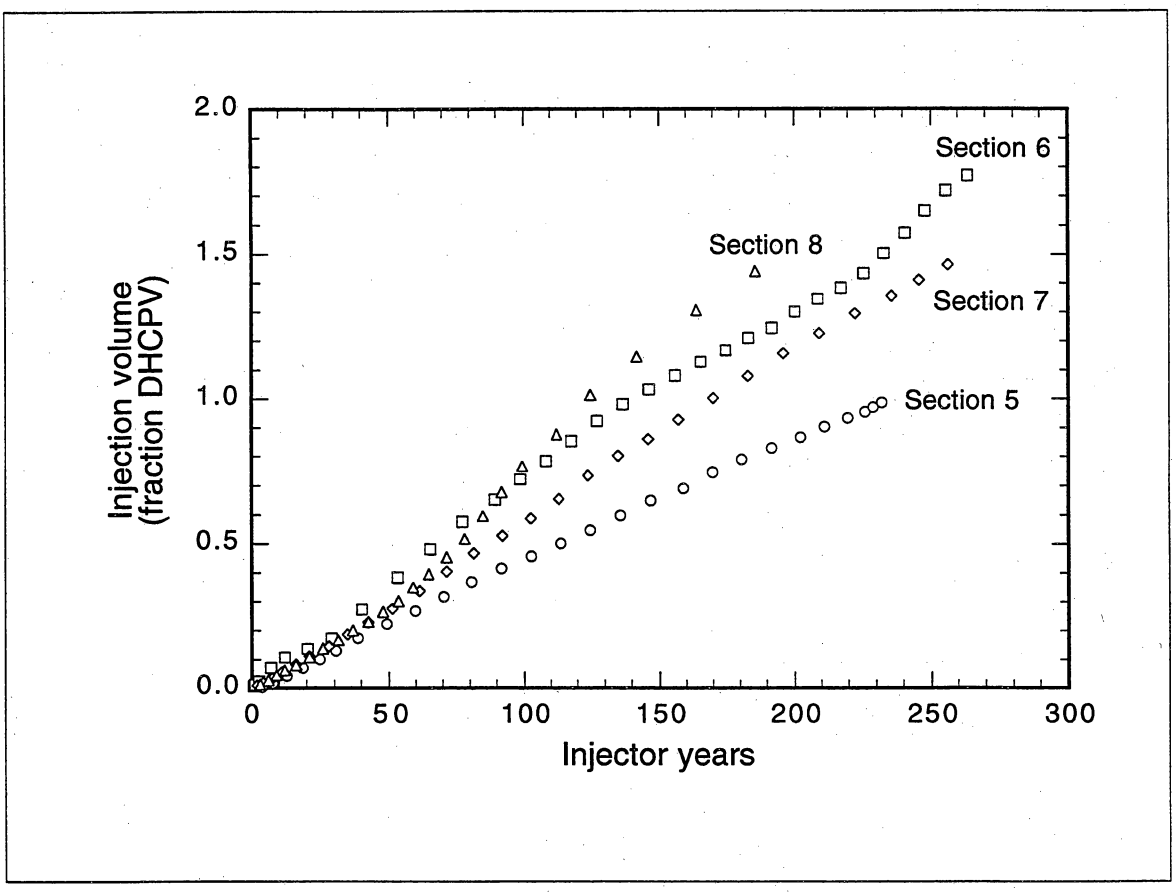

Figure 11. Cumulative water injection for sections 5–8 in the South Cowden field.

The South Cowden field provides an opportunity to test these models and injectivity predictions.

The total injection rate in the field changed significantly with time due to the changing number of active injection wells. A convenient way to visualize the average injectivity per well is to graph the cumulative injection against the cumulative number of "injector years," the cumulative number of years each injector is active, summed for all injectors in an area (fig. 11). The slope of each line is the average injectivity expressed as a fraction of the DHCPV of the area injected per injection well, per year. The South Cowden injectivities ranged from 0.0043 in section 5 to 0.0078 in section 8, with an average of 0.006 DHCPV/well-year.

Injectivity and oil displacement are affected by the density and arrangement of wells. Thus, it is important to reproduce these factors in flow modeling.

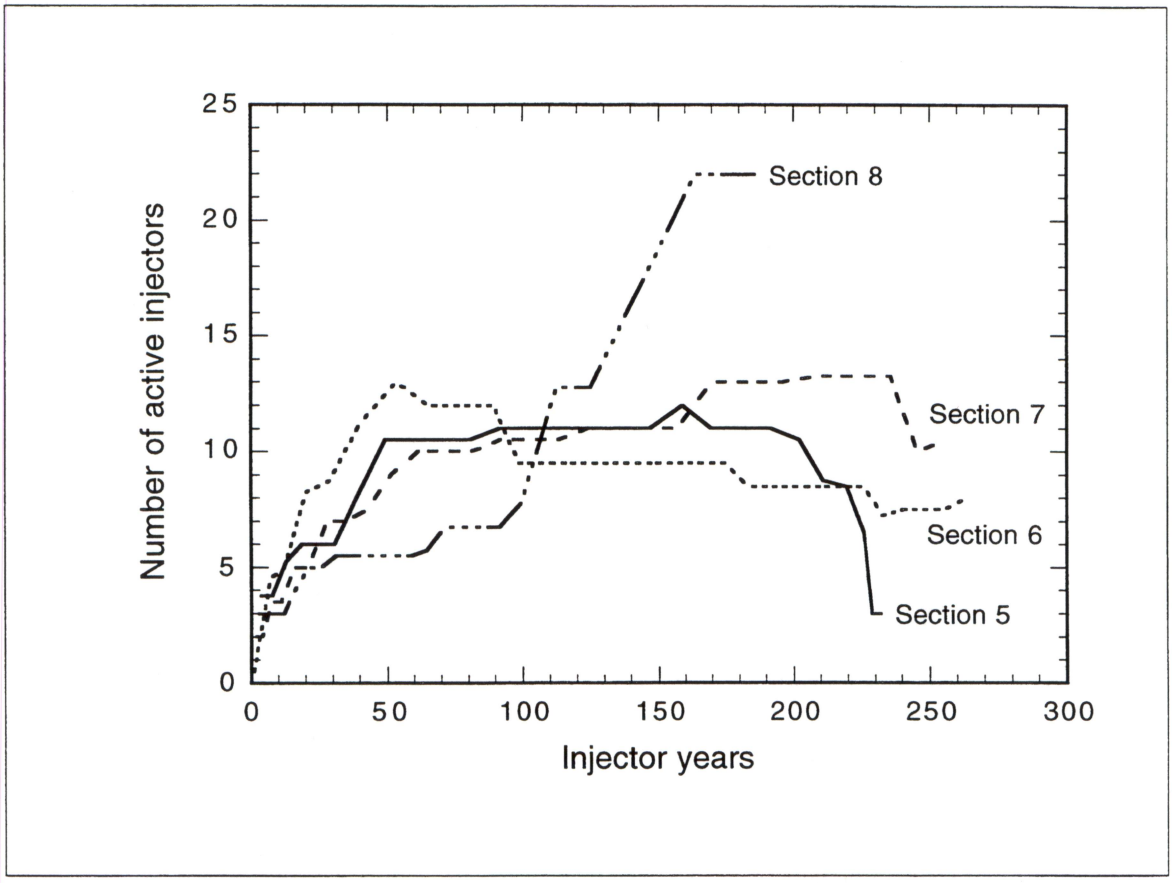

Figure 12. The number of active injectors in sections 5–8 of the South Cowden field.

Two parameters that characterize well density and arrangement in the South Cowden field are the number of injectors per unit area (fig. 12) and the injector-producer ratio (fig 13). Both parameters changed with time and location; the injector density averaged about ten injectors per section and the injector-producer ratio averaged about 0.6.

Some areas in sections 5–8 are currently at 10-acre spacing, but there are undrilled 10-acre locations; the average spacing during the waterflood was about one well per 24 acres. The close spacing aids in the mapping of high-frequency cycles and the interpolation of properties between wells.

Injectivity and oil displacement are also affected by the well completion strategy. The South Cowden field contains open-hole completions and cased wells with selective perforations. Completion data were available for the Moss Unit, indicating that the time-weighted average of completions in

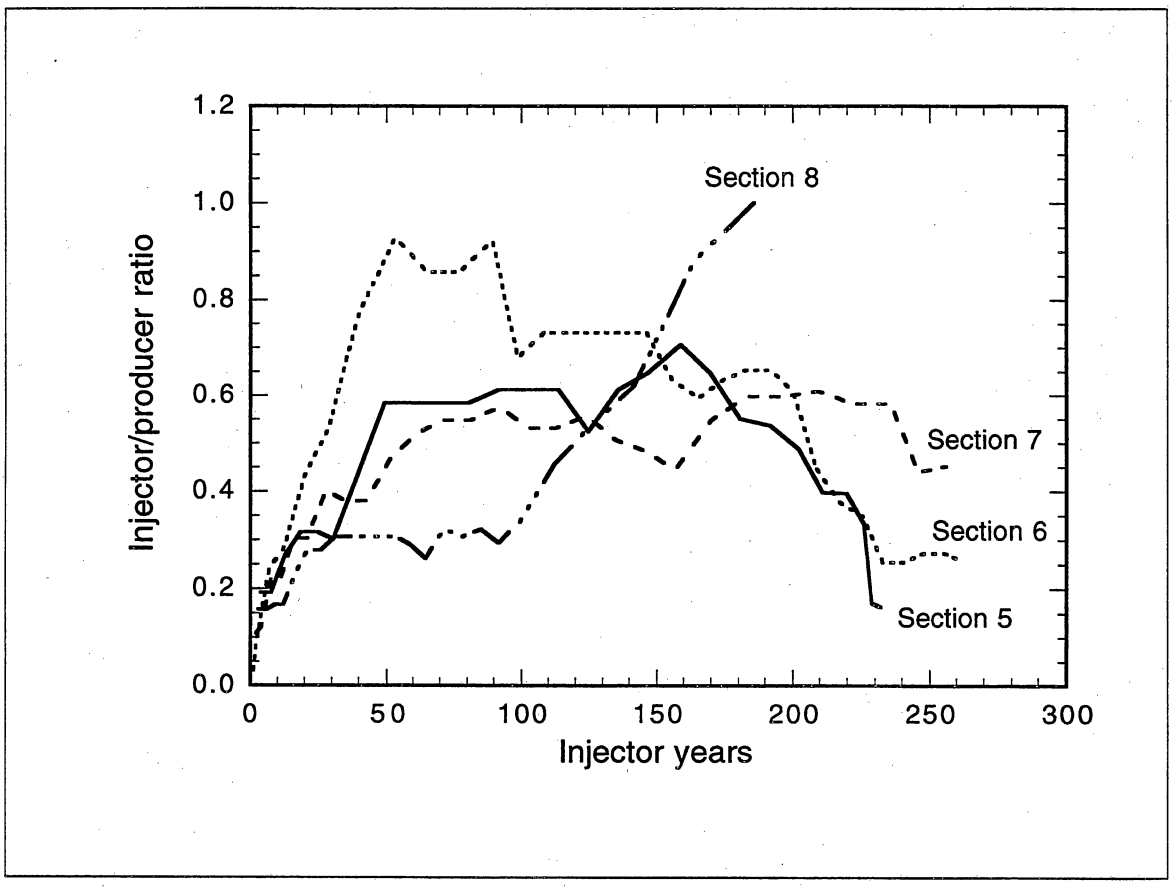

Figure 13. The injector-producer ratio in sections 5–8 of the South Cowden field.

producers started 5 percent of the way down from the top of the formation to the "H" marker and ended at 56 percent. In injectors the average completion went from 10 to 50 percent. Thus, only the top half of the potentially productive formation was completed in the Moss Unit. The higher-porosity rock tends to be in the top of the formation, so more than half of the pore volume is completed. Nevertheless, there may be significant unswept oil in the bottom of the formation, and recovery may be improved by simply deepening the wells. This additional recovery is estimated later in the report. Many wells have gaps between the perforations, but this was ignored in the waterflood simulations; the wells were considered to be completely open to the formation between the topmost and bottommost perforation.

Heterogeneity Modeling

Five different sets of flow models were created, based upon different approaches to modeling reservoir heterogeneity: (1) a "uniform" model with completely homogeneous properties, (2) a "constant-layer" model composed of homogeneous layers each with different properties, (3) a "smooth-layer" model constructed with smooth interpolation of vertically averaged properties within each layer, (4) a "stochastic-layer" model constructed with stochastic simulation of vertically averaged properties within each layer, and (5) a "direct-stochastic" model constructed with three-dimensional stochastic simulation directly from foot-by-foot well data (table 1). One of the objectives of the study was to evaluate three of these approaches: smooth-layer, stochastic-layer, and direct-stochastic. The other two approaches, uniform and constant-layer, are generally considered obsolete, but they were included in the study for comparison purposes.

	Number of layers	Layer thickness (ft)	Number of areal grids	Areal grid size (ft)	Description
Uniform	12	variable	22 x 22	60 x 60	completely homogeneous averaged properties
Constant-layer	12	variable	22 x 22	60 x 60	homogeneous averaged properties for each layer
Smooth-layer	12	variable	22 x 22	60 x 60	smooth interpolation of vertically averaged properties in each layer
Stochastic-layer	12	variable	22 x 22	60 x 60	stochastic simulation of vertically averaged properties in each layer
Direct-stochastic	40	6.5	11 x 11	120 x 120	3D stochastic simulation directly from ft-by-ft well data

Table 1. Summary of the five heterogeneity-modeling approaches used and the five sets of waterflood-simulation models produced.

Each of these models was constructed from log-derived porosity, permeability, and initial water saturation (Lucia, 1996). The layer-cake, smooth-layer, and stochastic-layer models also conformed to a geologic framework consisting of twelve high-frequency cycles (Lucia, 1996). The smooth-layer, stochastic-layer, and direct-stochastic models are described in the following sections.

Smooth interpolation of layer averages

The smooth-layer models were constructed with smooth interpolations of vertically averaged log-derived porosity, permeability, and initial water saturation for each of the twelve high-frequency cycles (Lucia, 1996; Ruppel and Bebout, 1996) in a 640-acre area centered on sections 5–8 (fig. 14).

The reservoir is dominated by a single petrophysical class, so the well-log models for permeability and initial water saturation can be written as simple functions of log-derived porosity (Lucia, 1996):

$$k = 2.04 \bullet 10^{6} \phi^{6.38} \tag{3}$$

and

$$s_{wi} = \begin{cases} \min\left(1 \text{ or } 2.63 \bullet 10^{-2} \phi^{-1.04}\right) & : \text{ above WOC} \\ 1 & : \text{ below WOC} \end{cases} \tag{4}$$

where ϕ and k are porosity and permeability, and the water-oil contact (WOC) is at a depth of 1,850 ft subsea. These properties were averaged by layer for each well using an arithmetic average for porosity, a porosity-weighted arithmetic average for saturation, and a one-third power average for permeability,

$$\bar{k} = \left(E\left[k^{\frac{1}{3}} \right] \right)^{3} \tag{5}$$

where $E[\bullet]$ is the expectation, or arithmetic-average operator. The one-third power average is a theoretically predicted approximate effective permeability

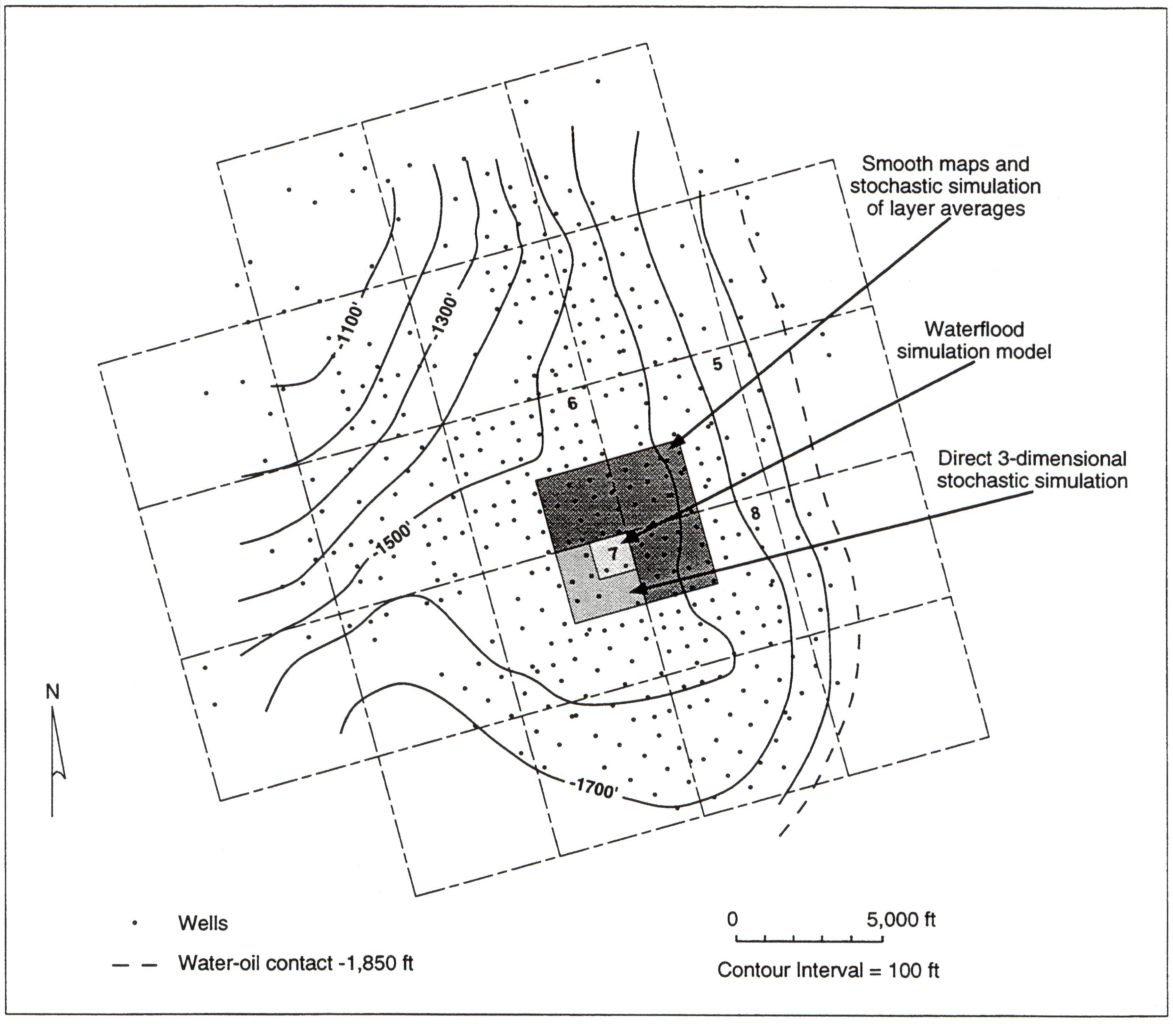

Figure 14. Location of heterogeneity and flow-simulation models.

for a log-normally distributed, three-dimensional, isotropic, and uncorrelated random permeability field (Romeu and Noetinger, 1995). This is reasonable because the permeabilities are approximately log-normal, flow within a layer is three dimensional, the core-scale vertical-to-horizontal permeability ratio (k_v/k_h) is within an order of magnitude of one (the geometric average of 3,000 measurements in 13 wells is 0.4), and carbonate outcrop measurements indicate that small-scale permeabilities are nearly uncorrelated within a single lithologic unit (Senger and others, 1991; Grant and others, 1994; Wang and others, 1994).

Individual well-log measurements of ϕ, k, and s_{wi} are of course perfectly correlated because they are computed directly from the log models (eqs. 3 and

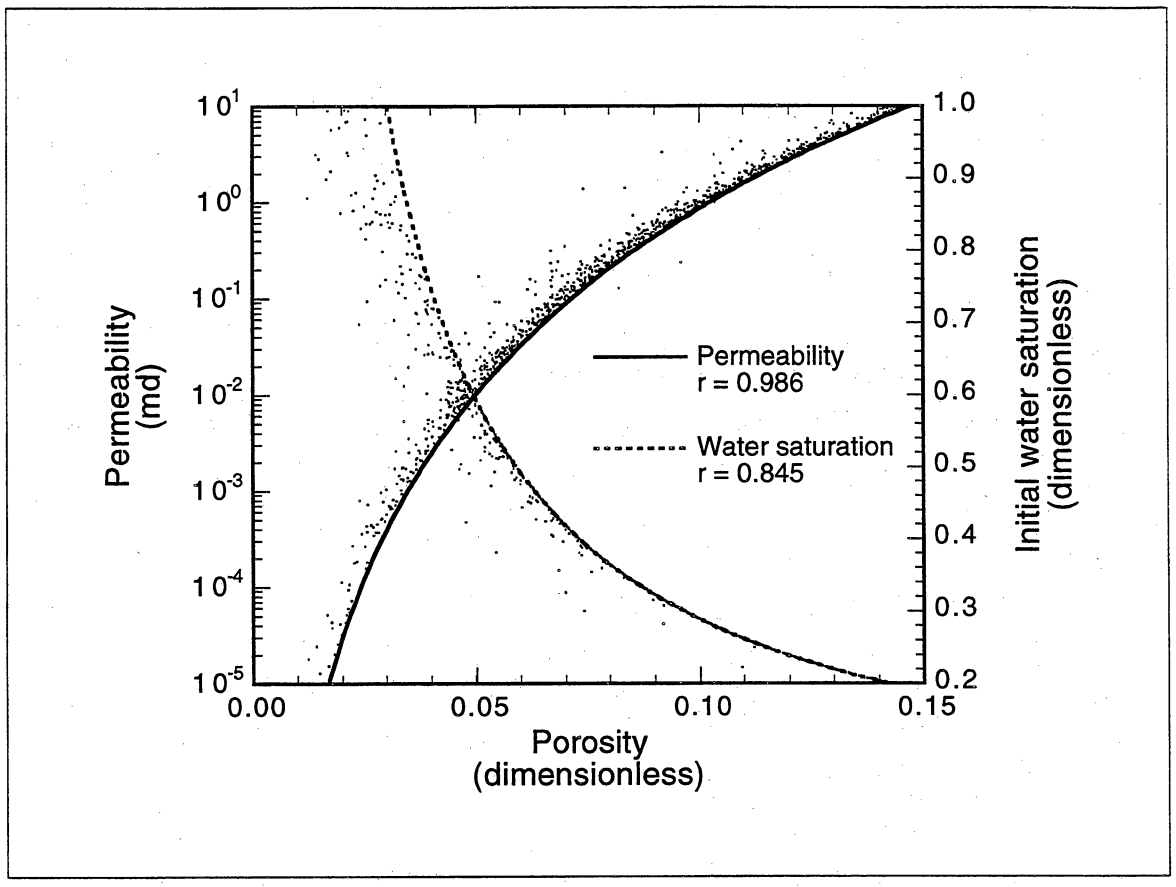

Figure 15. Layer-averaged porosities, initial water saturations, and permeabilities (points), with well-log models (curves).

4), but the layer-averaged properties are not because the relationships are nonlinear (fig. 15). The correlation coefficient between the logarithms of averaged ϕ and k is 0.986 and between the logarithms of averaged ϕ and s_{wi} is 0.845. However, these correlations are merely the outcome of averaging nonlinearly related properties and are not directly related to the actual correlation between these properties in the reservoir. The correlations between ϕ, k, and s_{wi} at the core-plug scale are certainly much smaller; the correlations between vertically averaged properties are not known but are probably smaller as well.

The well-log models are power laws of ϕ, k, and s_{wi}, so the logarithms of these properties are linearly related. Thus, it was natural to make the maps using logarithms of the layer-averaged properties followed by taking antilogarithms of the resulting interpolations. This procedure had the additional benefit that

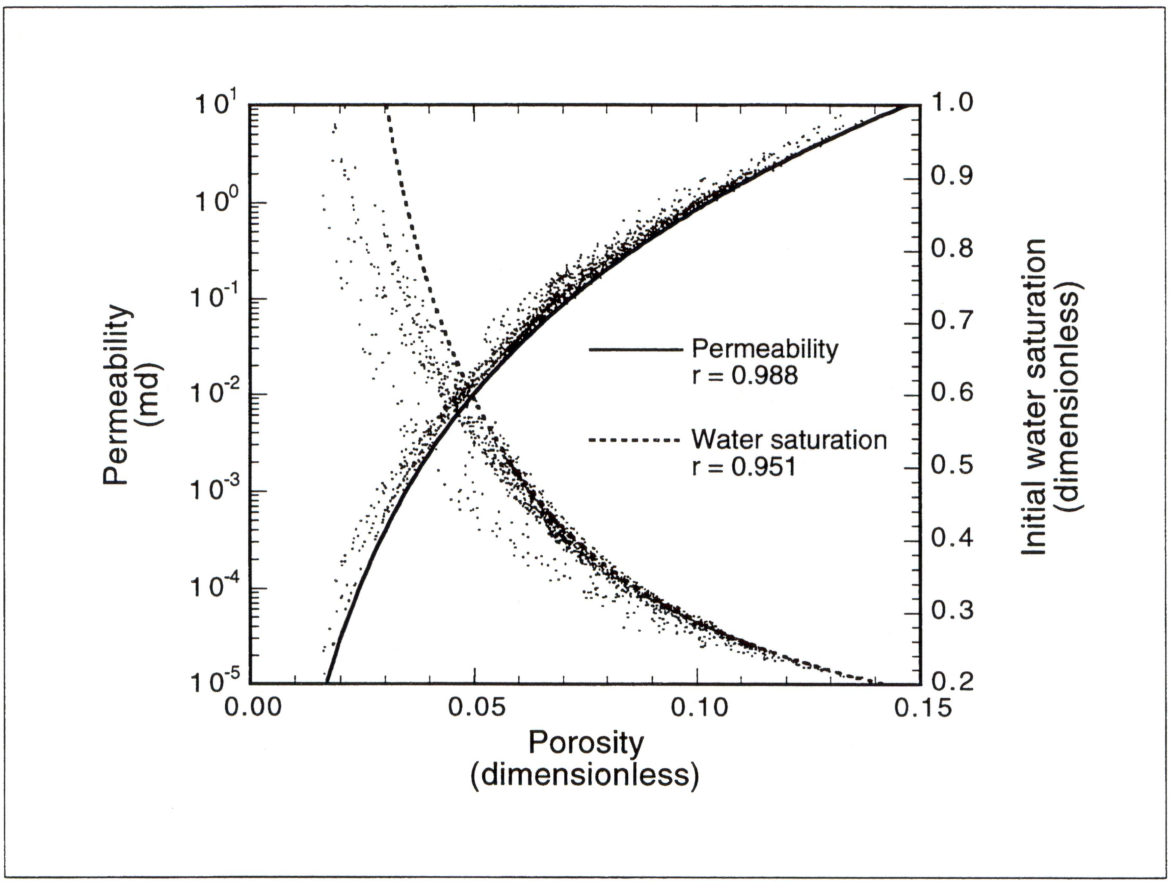

Figure 16. Porosities, initial water saturations, and permeabilities generated by smooth interpolation of layer-averaged well-log measurements (points, only every fourth point shown for clarity), with well-log models (curves).

negative values could not occur in the final maps. The properties generated this way are correlated with each other similarly to the control points (fig. 16; compare with fig. 15).

Two additional sets of maps were constructed by applying the log models to (1) calculate k and s_{wi} directly from the ϕ maps, and (2) calculate ϕ and s_{wi} directly from the k maps. These maps were very similar to the independently interpolated ones, but the properties were perfectly correlated. Maps of s_{w}- were set equal to s_{wi}. The residual oil saturations were computed from s_{wi} by application of the s_{oi}-s_{or} models described previously. Flow model properties were selected from a 40-acre area of each map (fig. 14) to create a 22-by-22-by-12 grid system (fig. 17).

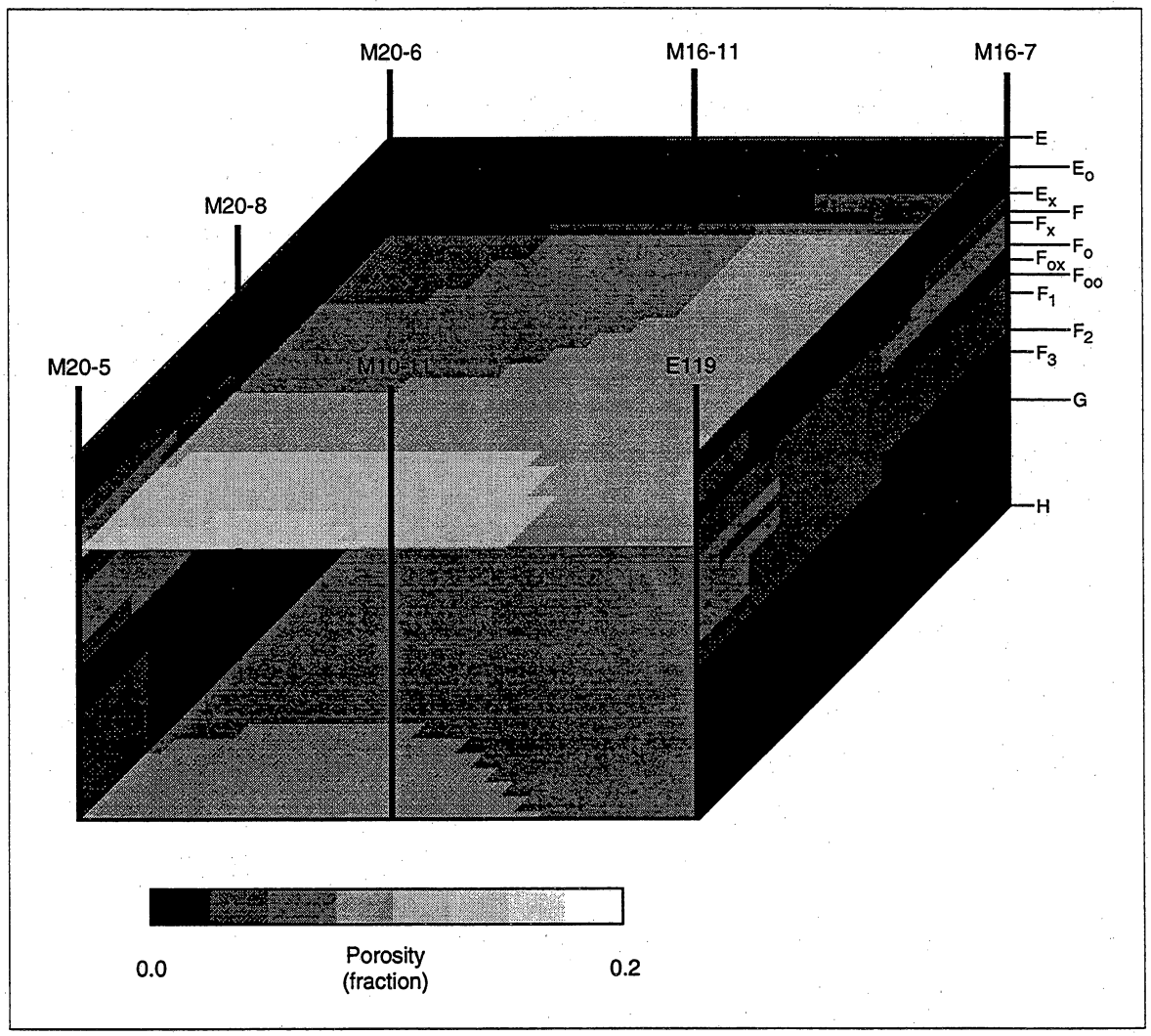

Figure 17. Porosity grid (see fig. 14 for location) generated by smooth interpolation of layer-averaged well-log measurements. The well locations are approximate. The model is 1,320 ft square and 300 ft thick.

Stochastic simulation of layer averages

A stochastic-layer approach was used to construct a more heterogeneous version of the high-frequency cycle based model using the same layer definitions and the same layer-averaged properties used in the smooth-layer model. The simulation method consisted of the following steps: (1) transform the data to standard gaussian form, (2) measure and model the variograms and cross variograms, (3) use the turning-bands method to generate multi-gaussian realizations conditioned to the variograms and the transformed control points, and (4) back-transform the resulting maps.

The layers were simulated simultaneously, rather than separately, allowing the correlation of properties between layers to be modeled. Thus, it was necessary to model the variograms in three dimensions with horizontal position as the x and y coordinates and layer number as the z coordinate. The variogram model was isotropic horizontally, but anisotropic in cross section with the axis of anisotropy aligned with the layers. The auto-variograms and cross-variograms of the three properties were modeled simultaneously with the "linear model of coregionalization" (Isaaks and Srivastava, 1989) and two structures (figs. 18 and 19),

$$\gamma_{ij}(\mathbf{h}) = a_{ij}\gamma_a(\mathbf{h}) + b_{ij}\gamma_b(\mathbf{h}) \tag{6}$$

where $\mathbf{h}$ is the lag vector, γ_a and γ_b are the two variogram structures, and γ_{ij} is the auto- or cross-variogram for properties i and j. The constants a_{ij} and b_{ij} are elements of symmetric matrices $\mathbf{A}$ and $\mathbf{B}$, tuned to match the sills of the measured auto- and cross-variograms. Assigning the indices 1, 2, and 3 to the gaussian transforms of ϕ, k, and s_{wi} respectively,

$$\mathbf{A} = \begin{bmatrix} 0.4627 & 0.4465 & -0.4491 \\ 0.4465 & 0.4384 & -0.4383 \\ -0.4491 & -0.4383 & 0.4472 \end{bmatrix} \tag{7}$$

and

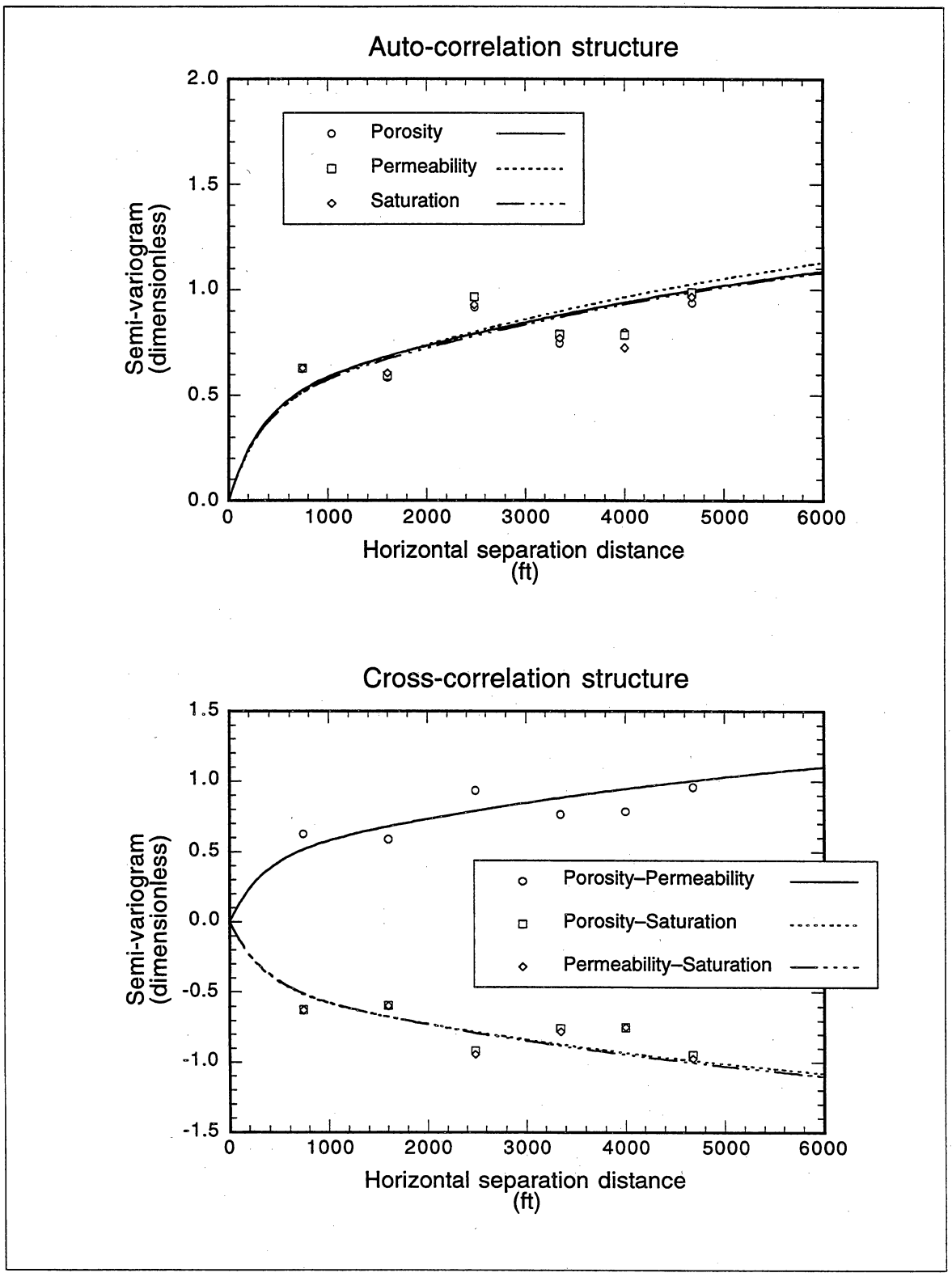

Figure 18. Horizontal auto- and cross-variograms for gaussian transforms of vertically averaged porosity, permeability, and initial water saturation from well logs. The measured variograms are shown with symbols, the models with curves.

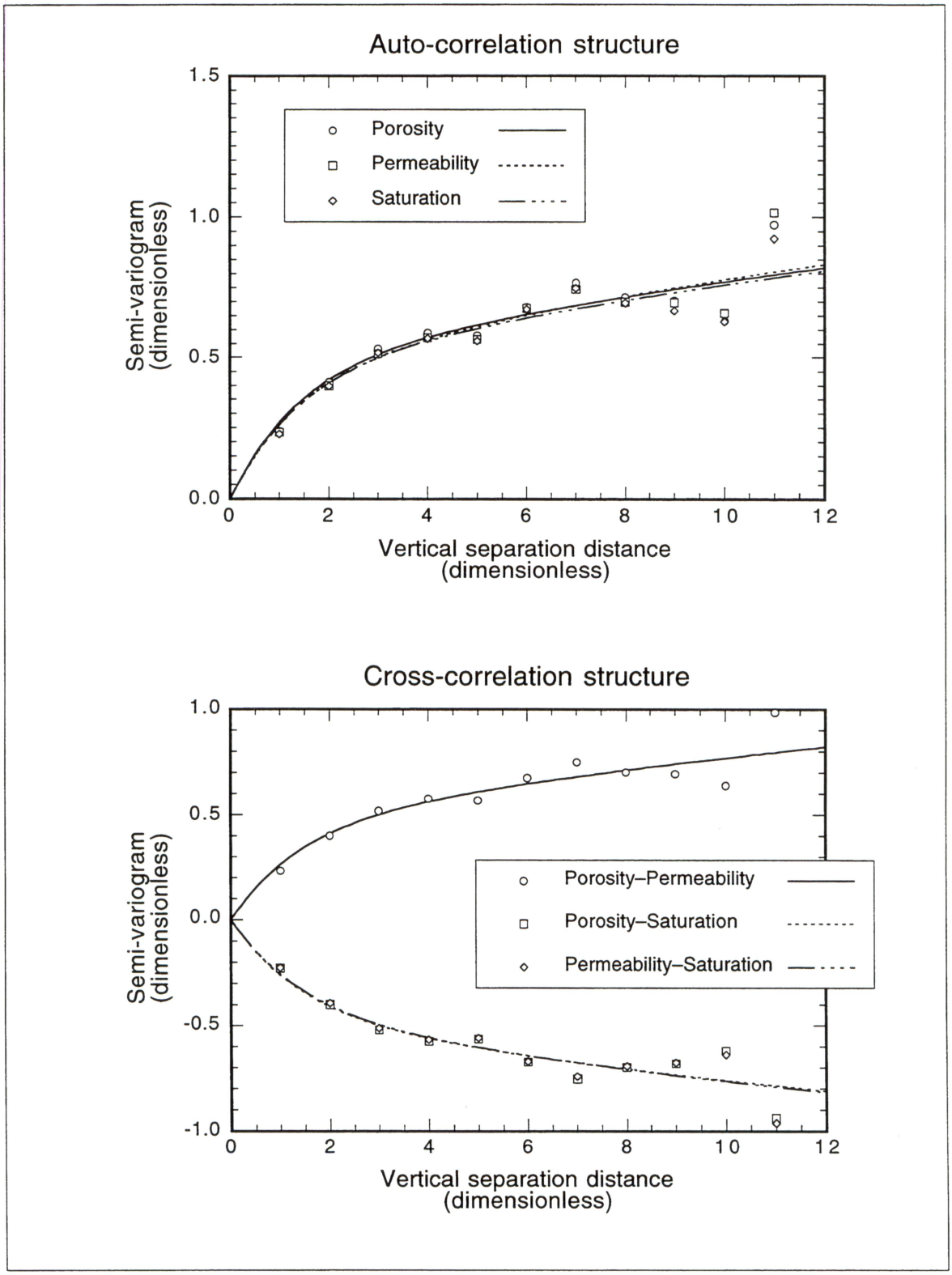

Figure 19. Vertical auto- and cross-variograms for gaussian transforms of vertically averaged porosity, permeability, and initial water saturation from well logs. The measured variograms are shown with symbols, the models with curves. The vertical "separation distance" is a dimensionless difference between layer numbers.

$$\mathbf{B} = \begin{bmatrix} 1.043 & 1.095 & -1.050 \\ 1.095 & 1.150 & -1.103 \\ -1.050 & -1.103 & 1.058 \end{bmatrix} \tag{8}$$

The two variogram structures were exponential with the "geometric model of anisotropy" (Isaaks and Srivastava, 1989) and range coefficients tuned to approximate the shape of the measured auto- and cross-variograms,

$$\gamma_a(\mathbf{h}) = 1 - \exp(-h/330) \tag{9}$$

$$\gamma_b(\mathbf{h}) = 1 - \exp(-h/6600) \tag{10}$$

and

$$h = \sqrt{h_x^2 + h_y^2 + (230h_z)^2} \tag{11}$$

where h_x and h_y are the horizontal components of the lag vector, in feet, and h_z is the dimensionless vertical component (layer number). The two structures have different ranges but the same anisotropy.

The auto- and cross-variograms of ϕ, k, and s_{wi} are nearly the same in any given direction, except for a negative sign on cross-variograms involving s_{wi}. The similarity results from two conditions: (1) the vertically averaged ϕ, k, and s_{wi} are strongly correlated, and (2) the gaussian transforms all have the same variance. The cross-variograms involving s_{wi} are negative because s_{wi} is anticorrelated with ϕ, and k.

These variograms and the gaussian-transformed control points were used to generate five conditioned realizations of cosimulated ϕ, k, and s_{wi}. The properties constructed this way are correlated with each other similarly to the control points (fig. 20; compare with fig. 16). The grid-block properties for waterflood simulation (fig. 21; compare with fig. 17) are much less smooth than those generated with smooth interpolation, and there is considerable variation between different realizations.

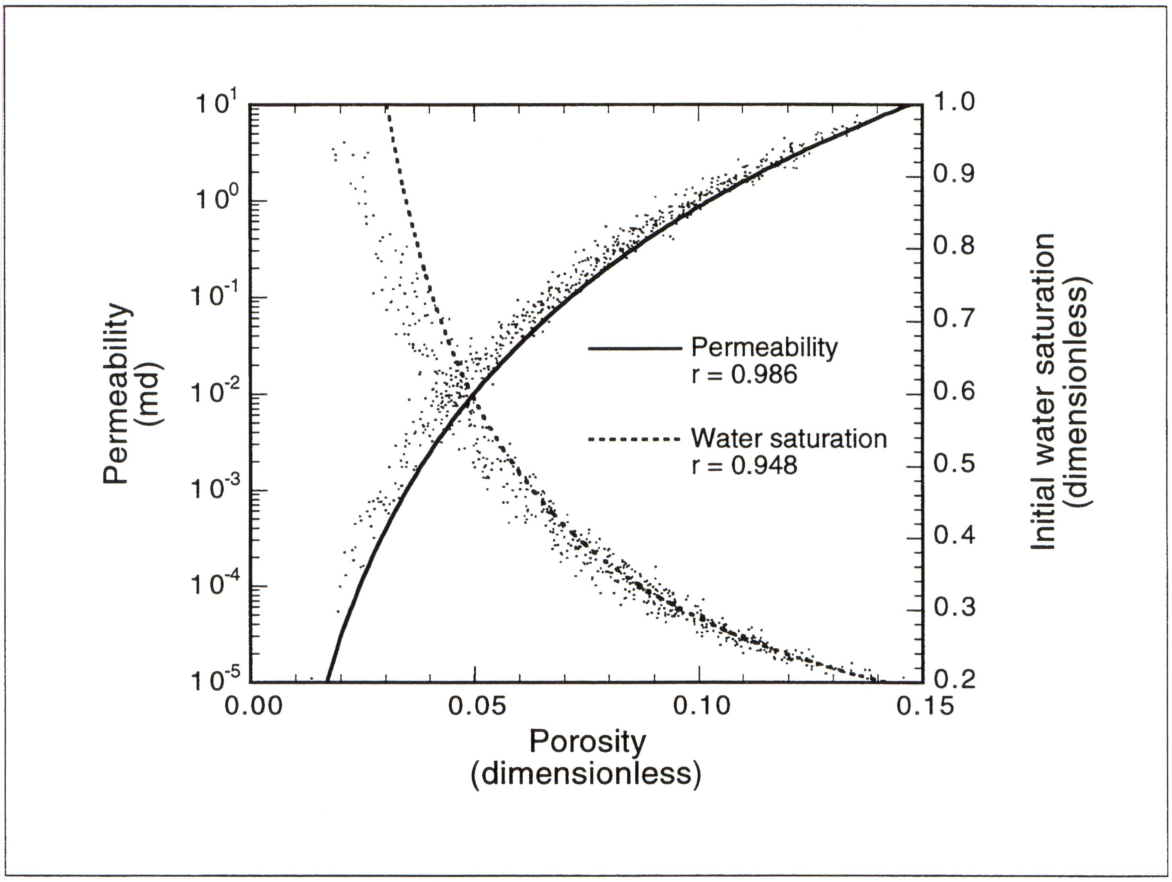

Figure 20. Porosities, initial water saturations, and permeabilities generated by stochastic simulation of layer-averaged well-log measurements (points, only every fourth point shown for clarity), with well-log models (curves).

Two additional sets of flow-model grids were constructed by applying the log models to (1) calculate k and s_{wi} directly from ϕ, and (2) calculate ϕ and s_{wi} directly from k. These realizations were very similar to the cosimulated ones, but the grid-block properties were perfectly correlated. In all of these models the immobile water saturation endpoints were set equal to s_{wi}. The residual oil saturations were computed from s_{wi} by application of the s_{oi}-s_{or} models described previously.

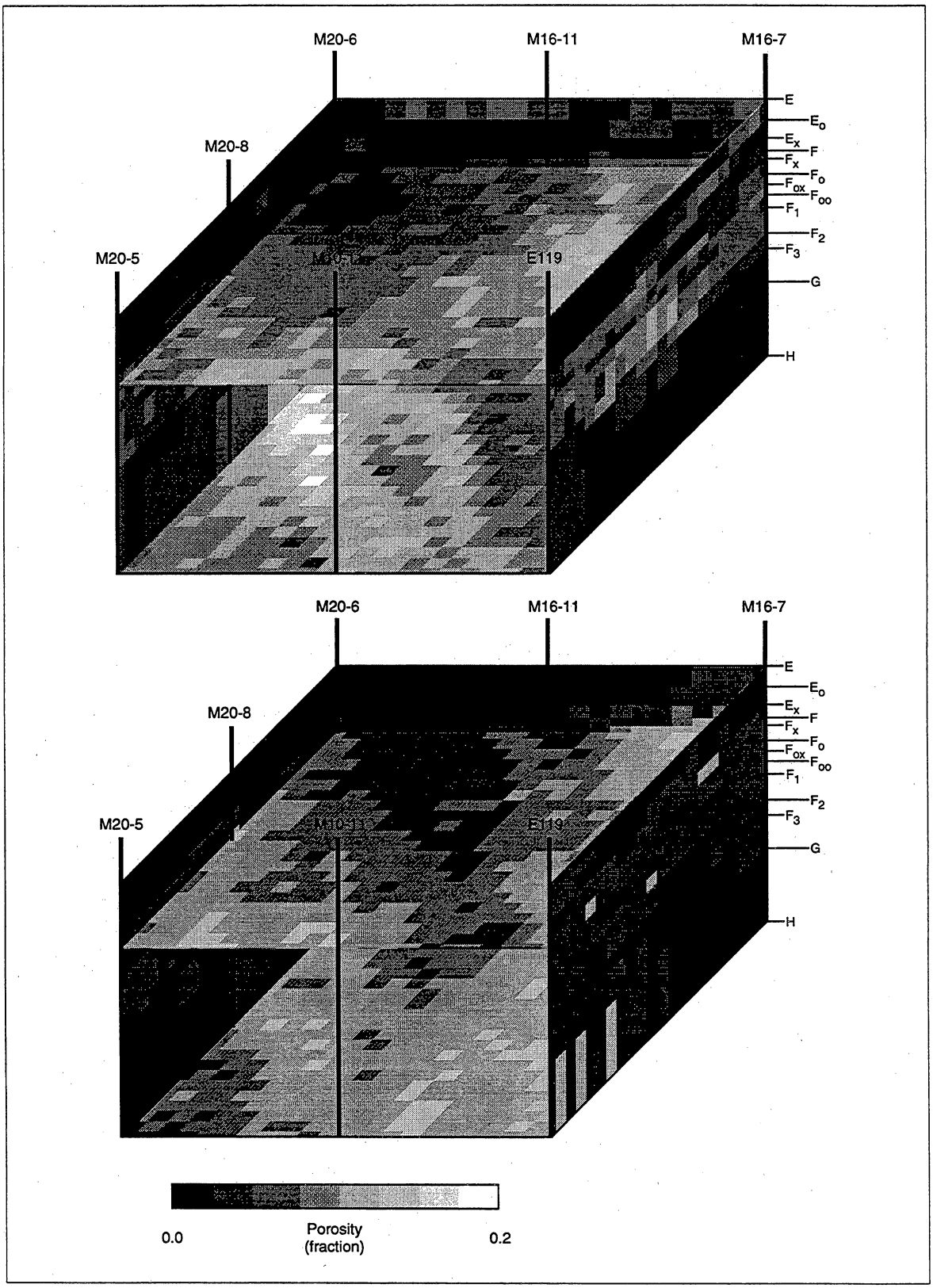

Figure 21. Two realizations of porosity for the waterflood simulation model (see fig. 14 for location) generated by stochastic simulation of layer-averaged well-log measurements. A total of five realizations were generated. The well locations are approximate. The model is 1,320 ft square and 300 ft thick.

Direct three-dimensional stochastic simulation

The direct-stochastic model was constructed using stochastic simulation applied to the foot-by-foot well-log data directly, eliminating the vertical averaging step of the smooth-layer and stochastic-layer models. The porosity data for all wells in the field with an adequate porosity log (fig. 22) was the starting point for the statistical analysis.

The data were converted to a "stratigraphically normalized" coordinate system where a linear stretch was applied separately to each high-frequency sequence (HFS) in each well so that the thicknesses of each HFS would appear constant and equal to its average for the field. This transformation ensures

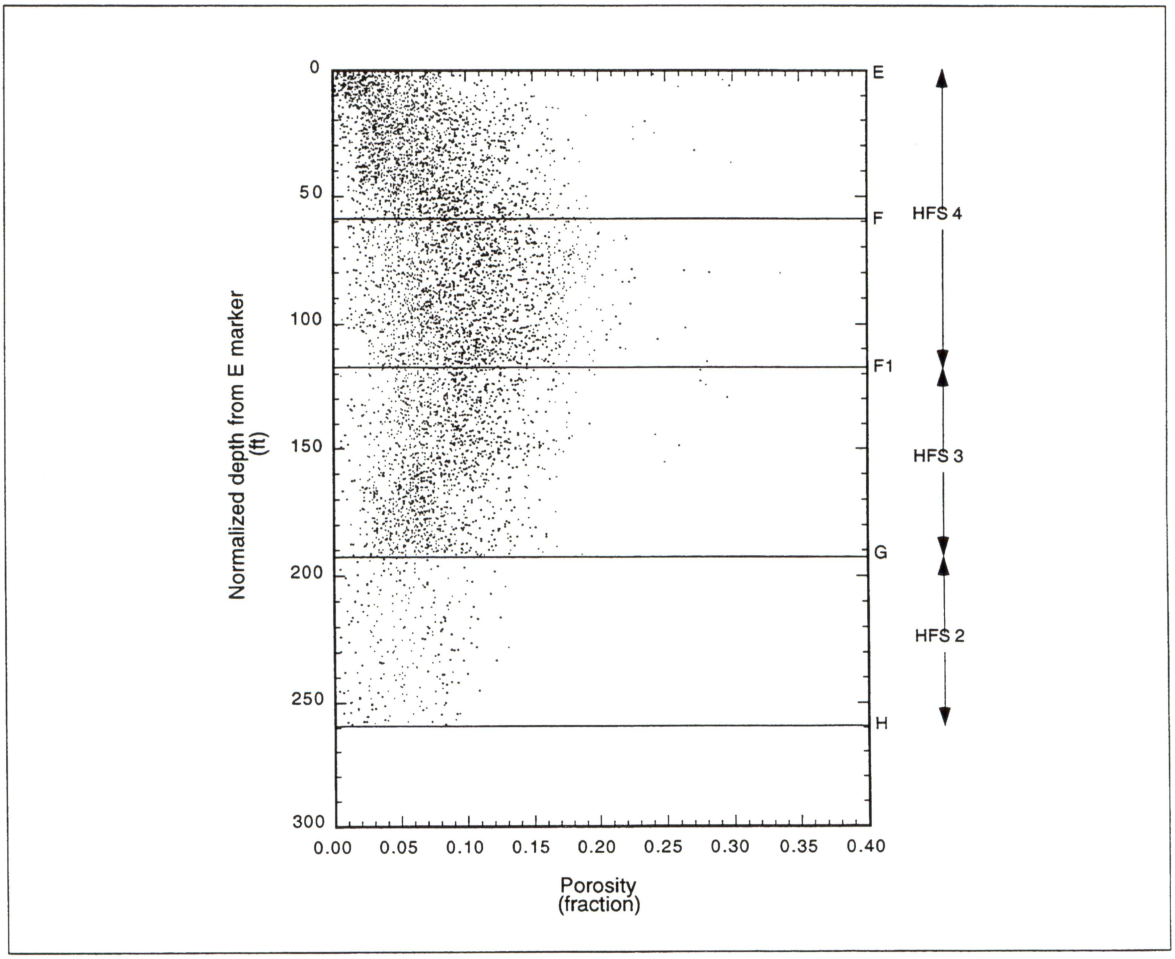

Figure 22. Well-log porosity data for all wells in the South Cowden field, using a "stratigraphically normalized" vertical coordinate; only every fifth point is shown for clarity.

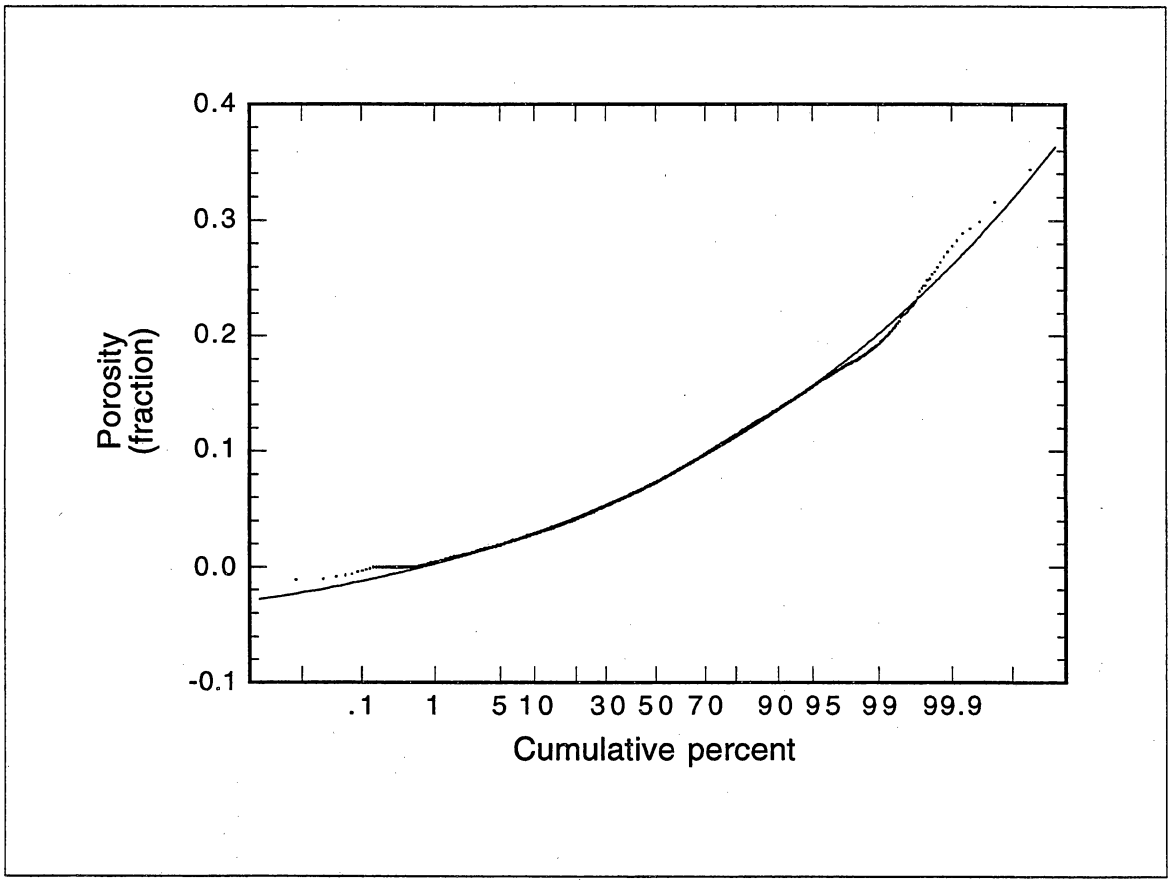

Figure 23. Well-log porosity data for all wells in the South Cowden field (points) and a model for gaussian transformation (curve).

that lateral correlation structure is measured and reproduced parallel to the sequence boundaries. A similar transformation could be applied at the more detailed high-frequency cycle level to obtain even better conformance to the stratigraphy, but those markers have not been determined for the entire field. Although there is considerable porosity variability, both laterally and vertically, a general trend can be seen: increasing porosity from the top of HFS 4 to a maximum in the bottom of HFS 4, and decreasing porosity through HFS 3 and 2.

The porosity distribution is not gaussian (fig. 23), but it can be modeled with a power law that was used to transform it to an approximately gaussian sample with zero mean and unit variance:

$$\phi_g = \frac{(\phi_l + 0.06)^{0.17} - 0.71}{0.037} \tag{12}$$

where ϕ_l is the well-log porosity and ϕ_g is the gaussian transform. The small amount of slightly negative porosities, presumably from well-log miscalibration, were included in the analysis and stochastic simulation; it was truncated before flow simulation.

Vertical and "horizontal" variograms were measured using the gaussian-transformed data (fig. 24). Indicator variograms were also measured (not shown) to verify that the random field is approximately bi-gaussian, a requirement of the gaussian simulation algorithms. A three-dimensional variogram model was fit to the measurements using three exponential structures that collapse to two structures in the vertical and horizontal directions:

$$\gamma(\mathbf{h}) = 0.24\gamma_{exp}(h_a) + 0.36\gamma_{exp}(h_b) + 0.40\gamma_{exp}(h_c) \tag{13}$$

$$\gamma_{exp}(h) = 1 - \exp(-h) \tag{14}$$

$$h_a = \sqrt{\left(\frac{h_x}{300}\right)^2 + \left(\frac{h_y}{300}\right)^2 + \left(\frac{h_z}{3}\right)^2} \tag{15}$$

$$h_b = \sqrt{\left(\frac{h_x}{300}\right)^2 + \left(\frac{h_y}{300}\right)^2 + \left(\frac{h_z}{70}\right)^2} \tag{16}$$

and

$$h_c = \sqrt{\left(\frac{h_x}{8500}\right)^2 + \left(\frac{h_y}{8500}\right)^2 + \left(\frac{h_z}{70}\right)^2} \tag{17}$$

where the subscripts *a*, *b*, and *c* refer to the short-, intermediate-, and long-range structures respectively. Each structure is anisotropic in cross section, aligned with the stratigraphy, and isotropic in plan view. The intermediate

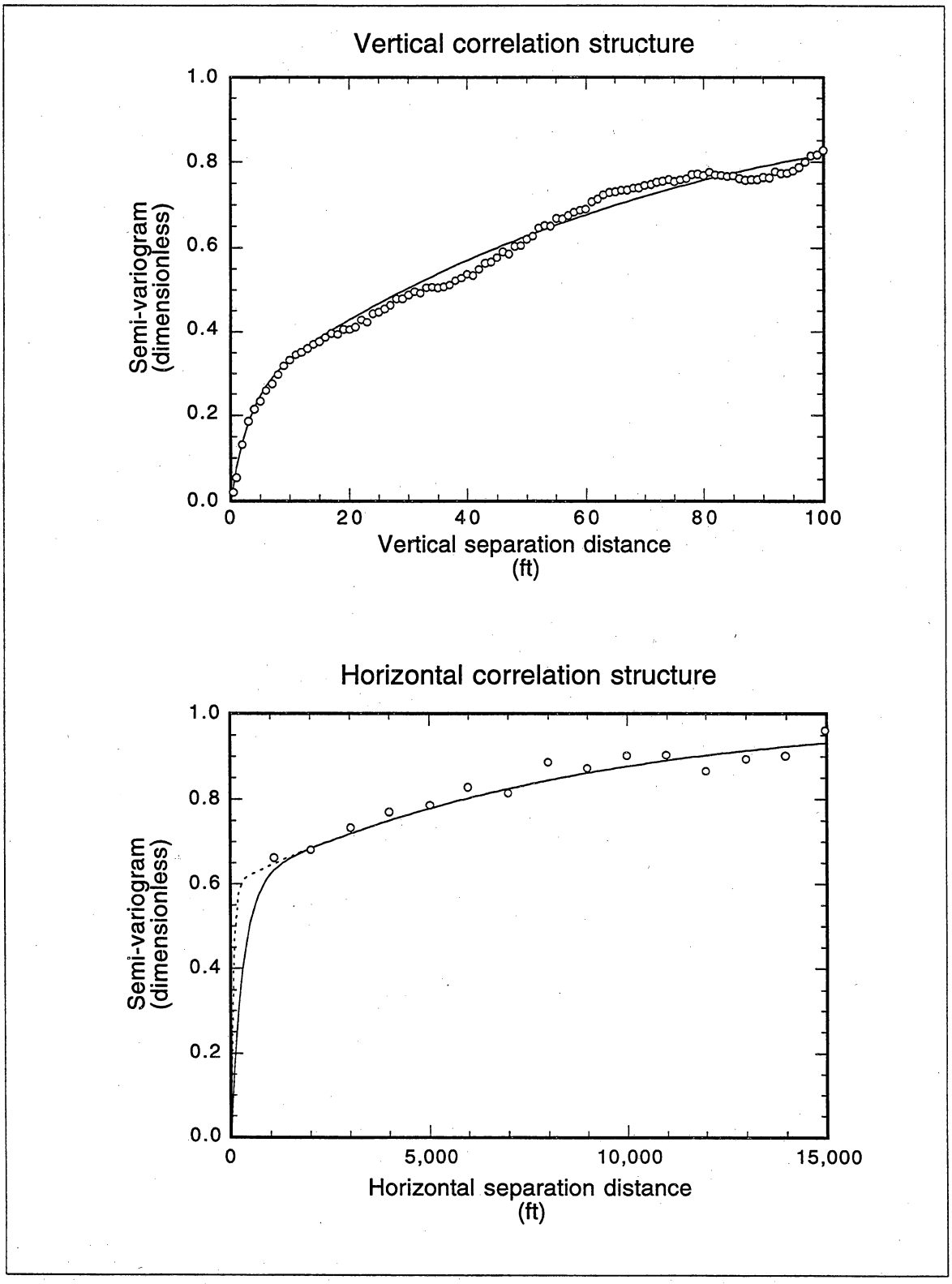

Figure 24. Vertical and horizontal variograms of gaussian-transformed well-log porosity. The measurements are shown as symbols, the models as curves; the dashed curve is an alternative model with a shorter horizontal range in the short-range structure.

structure has the same range as the small structure horizontally but the same as the large structure vertically; it models the difference in apparent long-range vertical and horizontal nuggets, 0.24 and 0.60 respectively.

There is some ambiguity in the short-range horizontal correlation structure because the lateral variogram cannot be measured at distances less than the well spacing. Extrapolation of the measured horizontal variogram to zero lag suggests a nugget of about 0.6, but this is inconsistent with the vertical variogram that has no nugget. Use of a horizontal variogram with a nugget together with a vertical variogram without a nugget would imply small-scale correlations that are stronger vertically than horizontally, something that does not seem reasonable from outcrop observations.

The model represented by eqs. 13–17 uses the largest possible range consistent with the data (300 ft) for the horizontal short-range structure. Another model was also tested using the smallest horizontal range possible without causing lateral correlations weaker than vertical (70 ft). The two models had almost identical effects in waterflood simulations, perhaps because of the grid size (120 ft) and the lack of rigorous scaleup calculations. Outcrop data suggest a higher degree of variability at the small scale than either of the exponential horizontal models, but the effects of this are probably not detectable in the 120 ft grid-block model.

A realization was constructed with sequential gaussian simulation (Deutsch and Journel, 1992) on a stratigraphic coordinate system with 44-by-44-by-520 pixels, each 60 ft square and nominally 0.5 ft thick, for a total slightly over one million pixels. The model covers 160 acres in the northeast quarter of section 7 and was conditioned to wells in that area. The realization was sampled vertically by 16 "wells," not in the same locations as the conditioning data, to verify that the vertical porosity trend was approximately reproduced (fig. 25; compare with fig. 24). The realization also matched the power-law porosity distribution, after back transformation (fig. 26). The horizontal variogram is

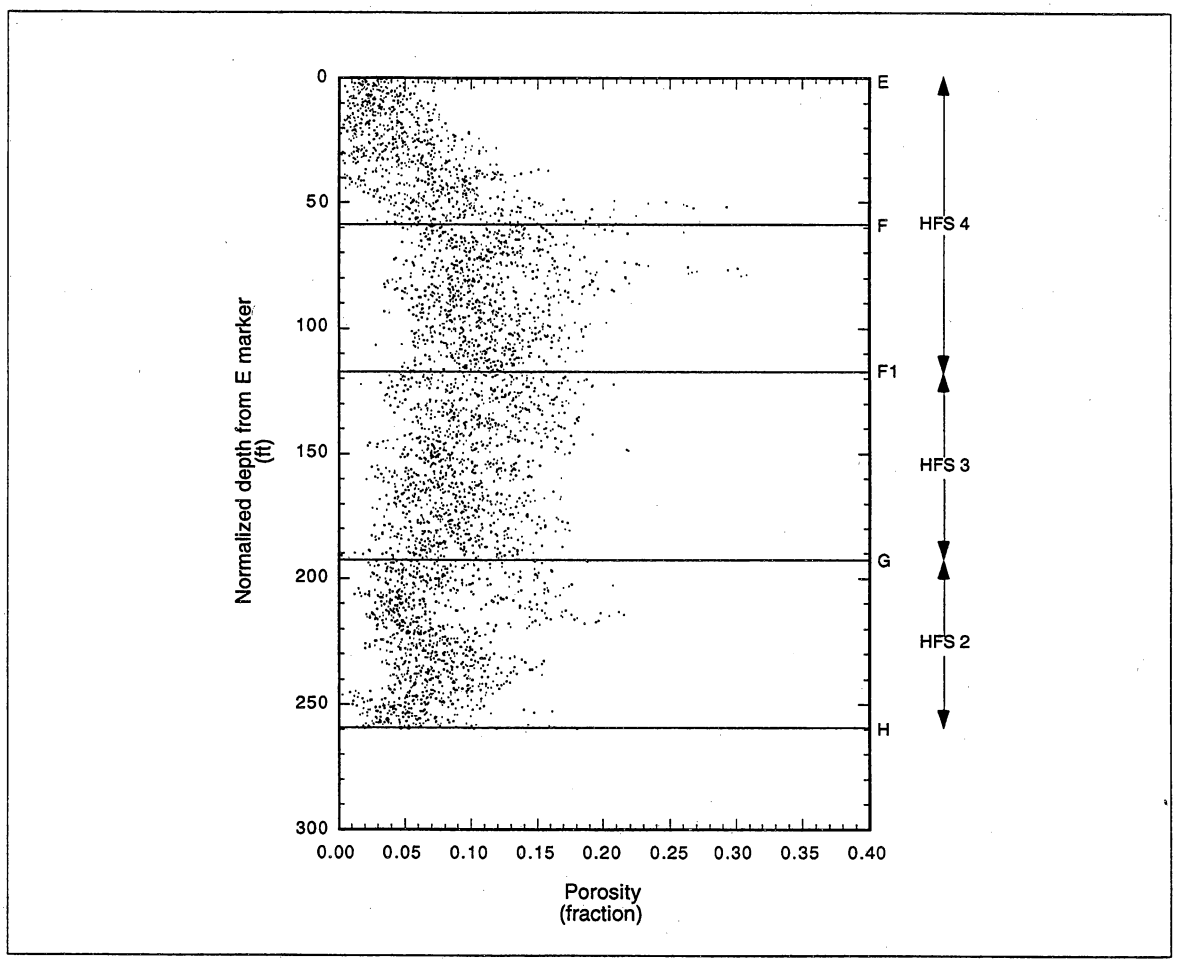

Figure 25. Simulated porosities for 16 "wells" displayed on a "stratigraphic" coordinate system; only every second point is shown for clarity.

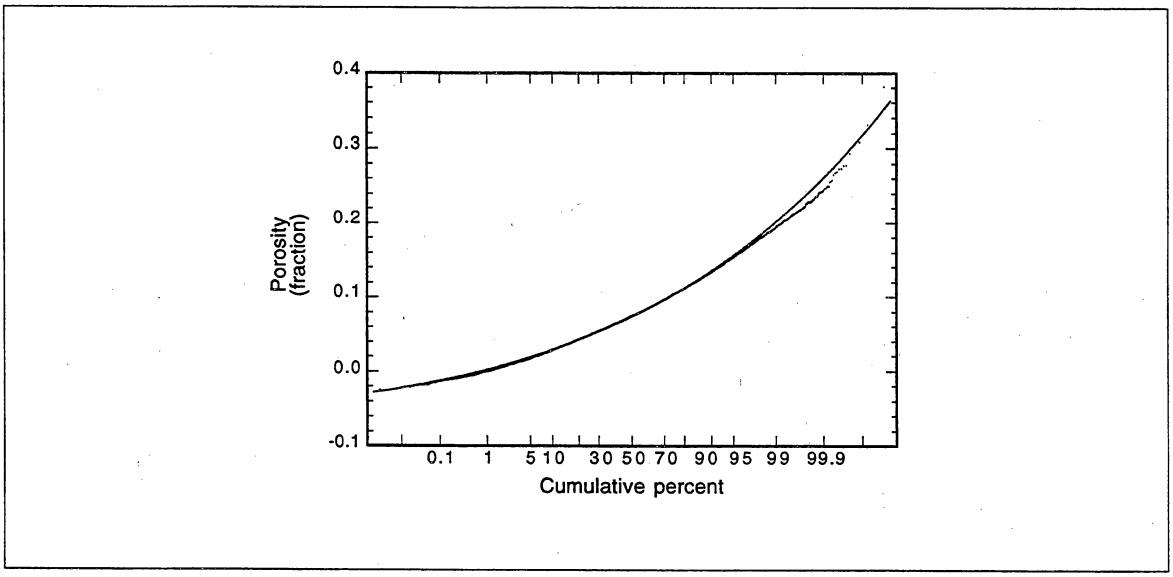

Figure 26. Simulated porosities (points) and a model of the porosity distribution (curve).

matched approximately to 1,000 ft; after that the fit degrades due to a well-known difficulty in reproducing long-range correlations on dense grids (fig. 27). The vertical variogram had the correct range, but the sill was too high by about 40 percent. This was necessary to achieve the desired overall variance.

Permeabilities and initial water saturations were calculated for each pixel by applying the well-log models; the immobile water saturation was set to the initial water saturation, and the immobile oil saturation was calculated from the initial-residual model. For this study the usual scaleup steps were skipped. The model was coarsened vertically, from 520 layers (0.5 ft thick) to 40 layers (6.5 ft thick), by simply sampling every 13th layer of pixels. It was coarsened areally, from 60 ft square pixels to 120 ft square grid blocks, by sampling every other pixel (fig. 28). Only the northeast quarter of the stochastic simulation, corresponding to Moss Unit tract 20, was used for flow simulation.

The constant-layer and uniform models

The constant-layer model was made by averaging thickness (h), thickness-weighted ϕ, and ϕh-weighted s_{wi} and s_{or} for each layer in the smooth-layer model. Layer permeabilities were calculated with a thickness-weighted geometric average. The geometric average is the theoretically predicted effective permeability for a log-normally distributed, *two-dimensional*, isotropic, and uncorrelated random permeability field (Romeu and Noetinger, 1995). The uniform model was made by averaging the thicknesses, thickness-weighted ϕ's, ϕh-weighted s_{wi}'s and s_{or}'s, and thickness-weighted permeabilities from the constant-layer model.

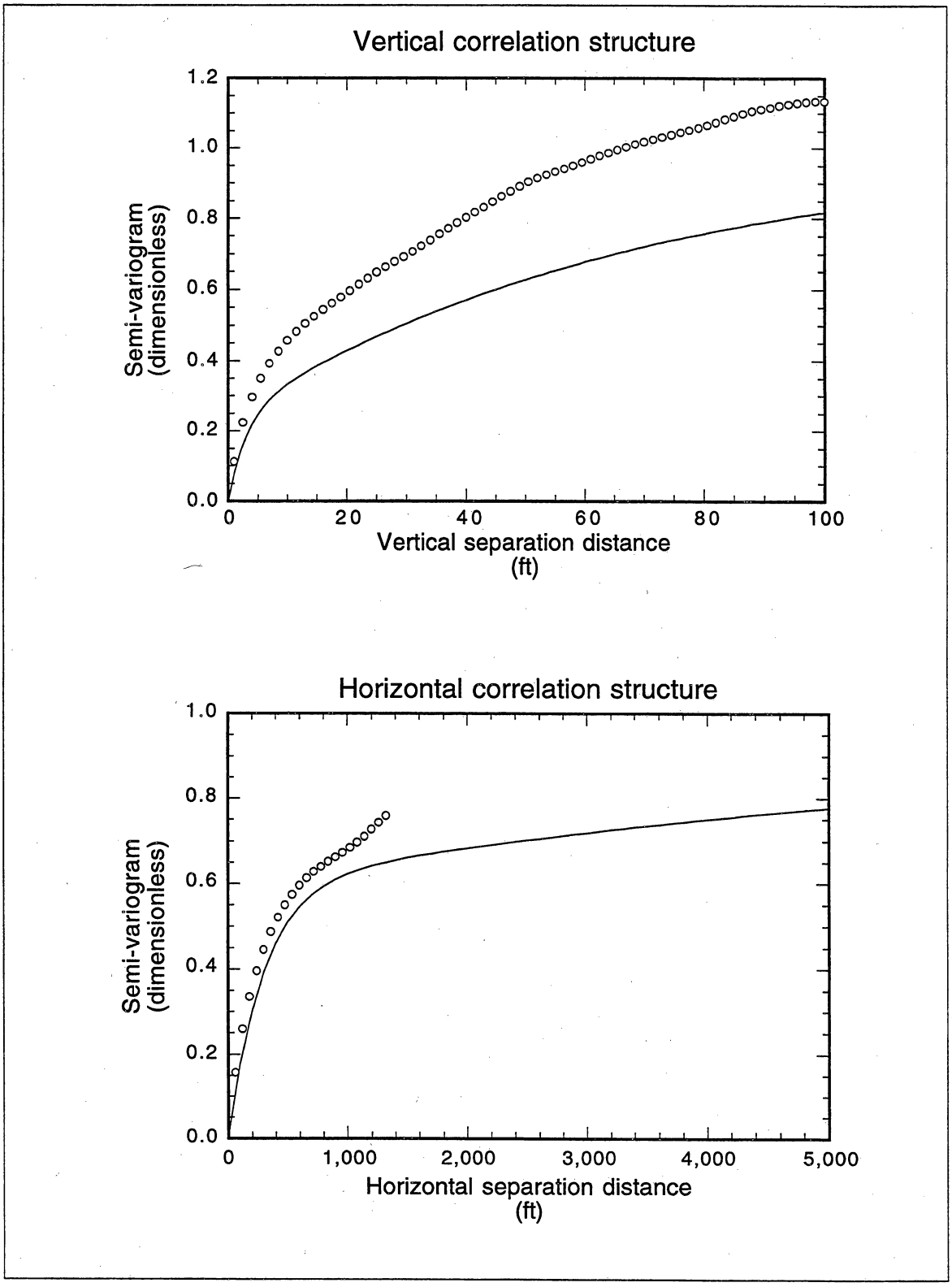

Figure 27. Vertical and horizontal variograms of simulated porosity. The measurements are shown as symbols, the models as curves.

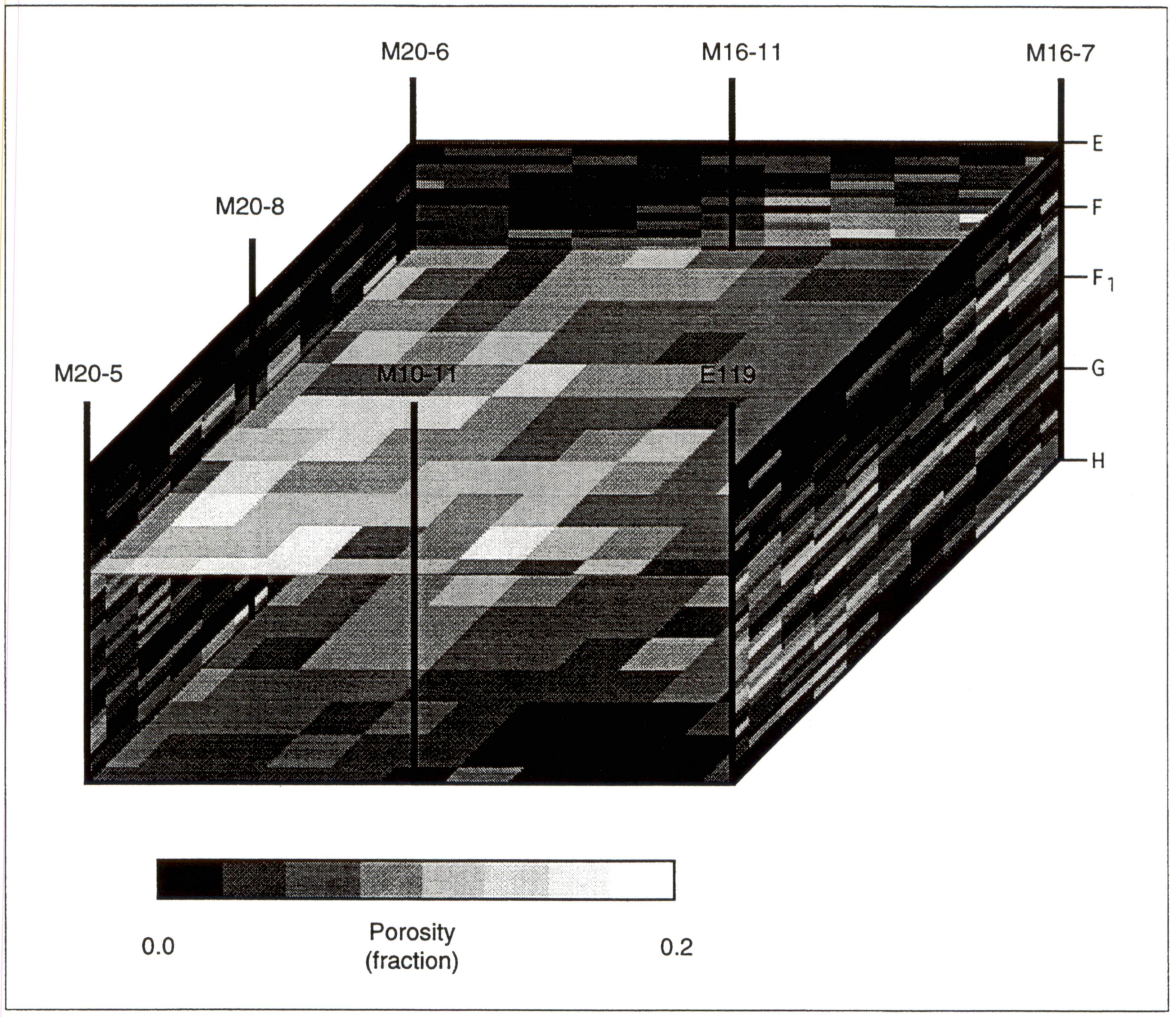

Figure 28. Porosity grid (see fig. 14 for location) generated by direct-stochastic simulation of foot-by-foot well-log measurements. The well locations are approximate. The model is 1,320 ft square and 260 ft thick.

Waterflood Simulations

Flow simulations were conducted with the UTChem software to explore the effects the different relative-permeability and heterogeneity models on waterflood performance predictions. UTChem was originally constructed as a chemical-flooding simulator (Pope and Nelson, 1978; Gupta and others, 1986), but for this study it was used in a black-oil mode with only two phases and two components: water and oil. The simulator incorporates a third-order flux-limiting scheme that results in reduced numerical dispersion relative to the standard single-point upwinding used in most simulators (Liu and others, 1994, 1995).

Model parameters

All the models covered a 40-acre-square area intended to represent the rock properties in the northeast corner of section 7 (fig. 14). The models extended from the "E" to the "H" marker; the "H" marker is near the water-oil contact in the model area. All of the waterflood simulations ignored the possible effects of a capillary transition zone, and the initial saturations were constructed with a height-independent log model (Lucia, 1996).

UTChem does not allow the thickness of a layer to vary arbitrarily in both horizontal dimensions, so a constant-thickness option was used. However, the layers could have different constant thicknesses; each was set to its average for the uniform, constant-layer, smooth-layer, and stochastic-layer models. This is a reasonable approximation because the layer thicknesses do not change dramatically in the model area; the standard deviation of thickness is less than 10 percent of the mean in most layers. The total thicknesses for these four models were all close to 300 ft, the average for the 40-acre-flow model area.

The direct-stochastic model was constructed with constant-thickness layers and had a total thickness of 260 ft, the average for the entire field. The difference in total thickness between the direct-stochastic model and the other four

had an effect on injectivity predictions; the per-well injectivities of a direct-stochastic model with 300 ft total thickness would have been larger by about 13 percent. There is probably not much effect on the recovery predictions compared on a DHCPV basis.

The porosities, permeabilities, water saturations, and endpoint saturations were obtained from the heterogeneity models. Permeability was considered isotropic horizontally; vertical permeabilities were obtained by application of a constant k_v/k_h ratio set to 1.0, 0.1, 0.01, or 0.001 in different runs.

The fluids were considered incompressible, and all volumes were expressed at subsurface conditions. The constant subsurface oil density (0.34 psi/ft) was estimated from the API gravity (34°) (Suter and others, 1961) and the volume factor. The water density (0.45 psi/ft) was similarly estimated from published correlations (Amyx and others, 1960). It made little difference in the model results whether gravity effects were turned on or off; it appears gravity has no important influence on water-oil displacement in the South Cowden reservoir. The fluid viscosities were considered constant: oil viscosity was set to 2.1 cp (from the relative permeability lab report), water to 0.8 cp (Suter and others, 1961). Capillary pressure was ignored.

The well arrangement is variable across the field and was not constant in time, but the current injection pattern in the model area is close to a line drive with the rows of injectors and producers on a 343° azimuth, parallel to the section lines. The average density of injectors in sections 5–8 is about ten per section, and the average injector-producer ratio is about 0.6. The well arrangement in the model was chosen to achieve a compromise between these factors (fig. 29). It is a line drive with extra producers to obtain an injector-producer ratio of one-half and an injector density of eight per section. Thus, the well arrangement in the model does not represent any particular 40-acre area of the field; it is a hypothetical model that approximates the average arrangement in sections 5–8. All sides of the model were approximated as no-flow boundaries. Thus, regional migration of fluids is

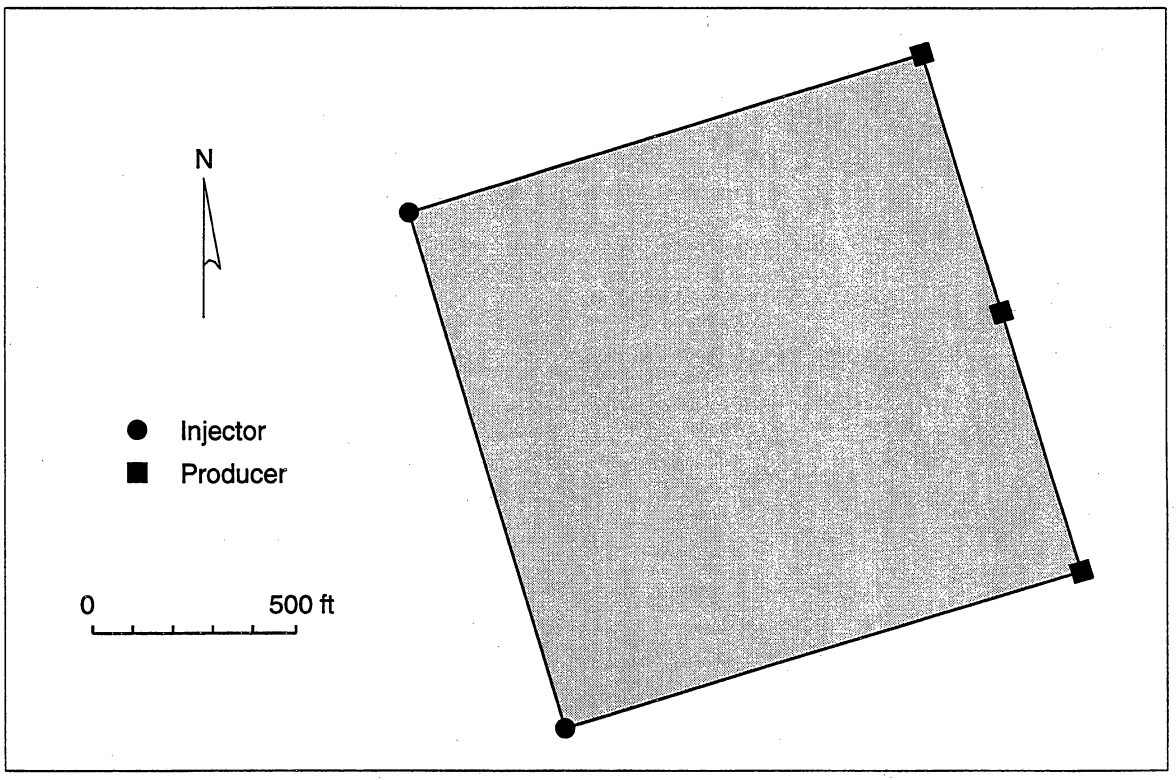

Figure 29. Well arrangement used in flow simulations. The model is 1,320 ft square (40 acres).

ignored, and the well arrangement is assumed to be an element of a repeated pattern.

The effective wellbore radius and skin for all wells in the model were set to one-half foot and zero respectively. This radius is larger than the original drilled hole size, but some of the older wells were shot with nitroglycerin, increasing the hole size by variable amounts, and many of the other wells were hydraulically fractured, increasing the effective hole size. No pressure-transient data were available to determine the effective wellbore properties, so there is an unavoidable uncertainty in the predicted injectivities and productivities.

In some runs, the wells were completed through the entire model. In others, only the top half of the total model thickness was perforated. The wells were operated at a constant bottom-hole pressure, 3,000 psi for injectors and 200 psi for producers.

Waterflood displacement results

The waterflood simulations are easiest to understand when the simplest models are examined first (fig. 30). These results explore the effects of well completions, relative-permeability models, and the three most homogeneous models: uniform, constant-layer, and smooth-layer. Among these variables, the well-completion strategy and the relative-permeability model had the most effect on oil displacement by waterflood. The heterogeneity model also had an important effect; each additional level of complexity reduced the waterflood recovery.

The effect of areal sweep due to well arrangement can be observed in a comparison of the uniform model with fully completed wells and a one-dimensional Buckley-Leverett calculation. There is very little difference between these cases, indicating that areal sweep in a hypothetical uniform South Cowden reservoir is not important to waterflood oil recovery; the completion strategy, affecting vertical sweep, is much more important.

In the case of fully completed wells, all the heterogeneity models approached the same ultimate recovery. All the displaceable oil was eventually recovered; none of the models have compartments isolated by zero-permeability barriers to permanently trap oil. However, the same ultimate recovery was obtained only after an impractical amount of water injection. The heterogeneity model had an important effect on the results in the economically important region between zero and several DHCPV injection. With partially completed wells the ultimate recoveries are not as clear, but they may also converge to the same result after even larger injection volumes.

Of the cases summarized in fig. 30, the one with partially completed wells, unsteady-state relative permeabilities, and the most heterogeneity had the best match of long-term field performance. None of the models predicted the early breakthrough time, or the poor recovery performance before about 0.8 DHCPV injection.

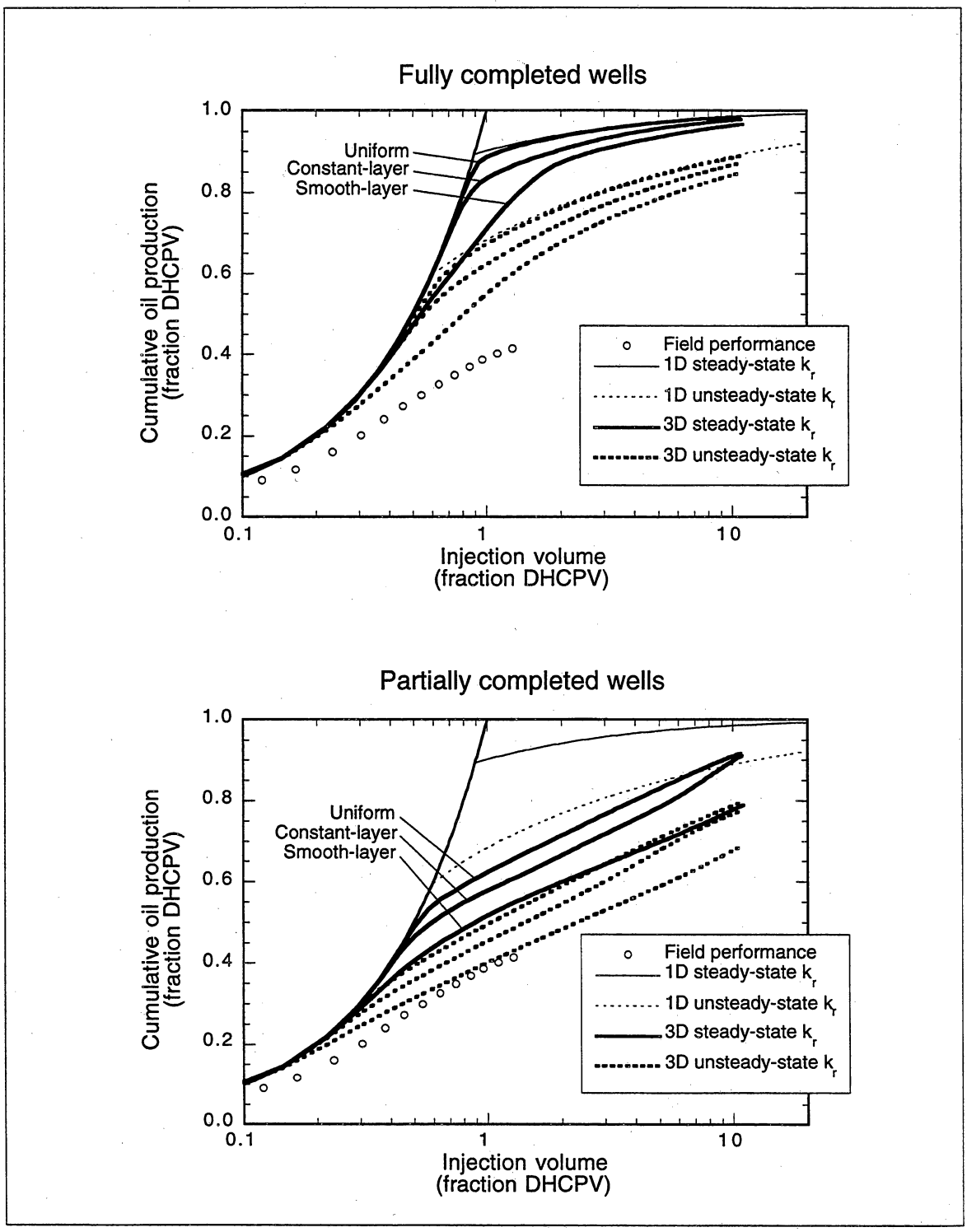

Figure 30. Field performance in sections 5–8, one-dimensional Buckley-Leverett predictions, and three-dimensional waterflood simulations using fully completed and partially completed wells. Each set of three simulations has a uniform case, a constant-layer case, and a smooth-layer case. The k_v/k_h ratio was 0.01, and the average s_{oi}-s_{or} model was used to convert field data to DHCPV.

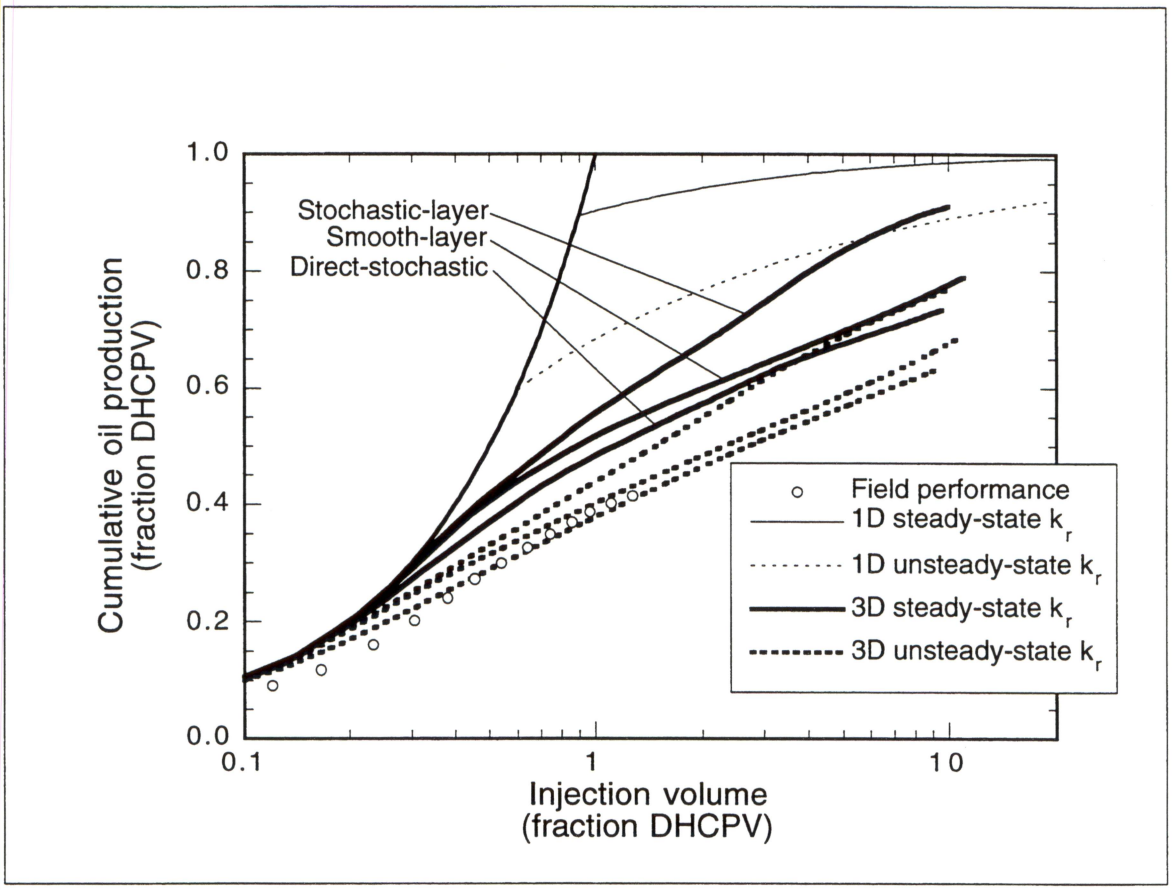

Figure 31. Field performance in sections 5–8, one-dimensional Buckley-Leverett predictions, and three-dimensional waterflood simulations using partially completed wells. Each set of three simulations has a smooth-layer case, a stochastic-layer case (average of five realizations), and a direct-stochastic case. The k_v/k_h ratio was 0.01, and the average s_{oi}-s_{or} model was used to convert field data to DHCPV.

More subtle effects were observed in a comparison of the three most complicated heterogeneity models: smooth-layer, stochastic-layer, and direct-stochastic (fig. 31). The stochastic-layer case is the average waterflood prediction from five realizations, but only one realization was used for the direct-stochastic case. The smooth-layer model had less oil recovery than the stochastic-layer model because it has more horizontal correlation; it has more continuous high-permeability channels and more persistent low-permeability barriers.

The direct-stochastic model predicted performance similar to the smooth-layer model, but with slightly less recovery and a somewhat better prediction

of breakthrough time. Recoveries were lower for the direct-stochastic model despite the fact that it has shorter horizontal correlations. The likely cause is the larger number of layers in the direct-stochastic model. Only the cases with the unsteady-state relative-permeability model were close to the long-term field performance, regardless of the heterogeneity model.

The k_v/k_h ratio had a small effect on waterflood recovery with fully completed wells, but it had a large effect with partial completions (fig. 32). In the partial-completion case, there is a trade-off between the effect of relative-permeability models and k_v/k_h ratios; the cases with steady-state k_r's and the two smallest k_v/k_h's had short-term performance similar to the unsteady-state k_r's and the two largest k_v/k_h's. Thus, it is difficult to determine both the relative permeability and the vertical permeability uniquely from comparison with waterflood-displacement observations alone. However, the models gave different long-term predictions, so it is important to estimate k_r and k_v/k_h independently from other sources for estimates of future behavior.

A comparison of performance predictions from the five different realizations of the stochastic-layer model gives an indication of the uncertainty due to unknown permeability variation between wells (fig. 33). A similar variability might have been observed with the direct-stochastic approach if multiple realizations of that model had been generated.

It made little difference in either the smooth-layer or stochastic-layer models whether porosity, permeability, and water saturation were generated separately or were perfectly correlated with one another through simple well-log models (fig. 34). However, this is no surprise, because the correlation coefficients were high in either case. The s_{oi}-s_{or} model had very little effect on simulation results compared in terms of DHCPV, but remember that it does have an effect when converting the observed waterflood performance data to a DHCPV basis (fig. 10).

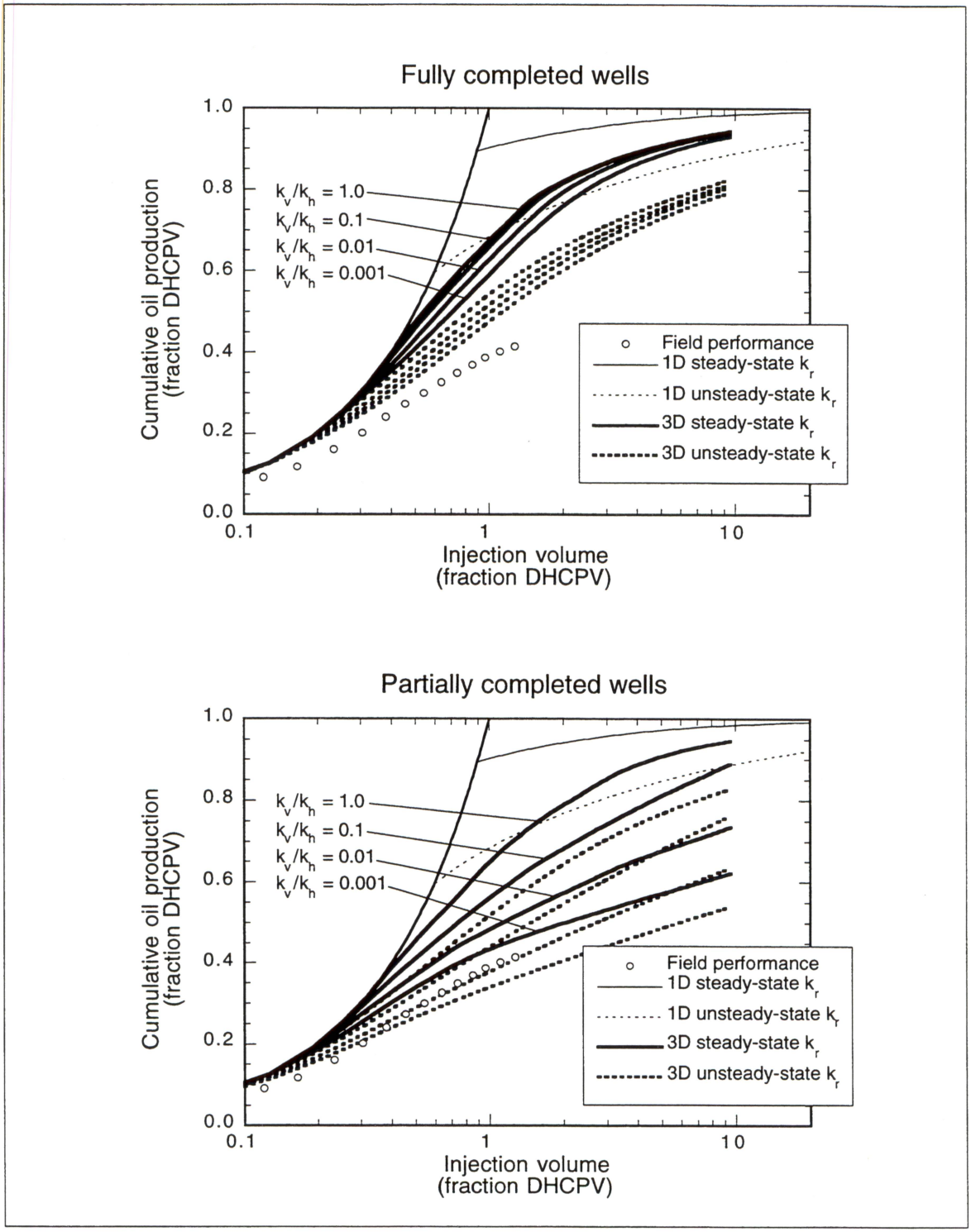

Figure 32. Field performance in sections 5–8, one-dimensional Buckley-Leverett predictions, and three-dimensional waterflood simulations using fully completed and partially completed wells. Each set of four simulations explores a range of k_v/k_h ratio from 0.001 to 1.0. The average s_{oi}-s_{or} model was used to convert field data to DHCPV.

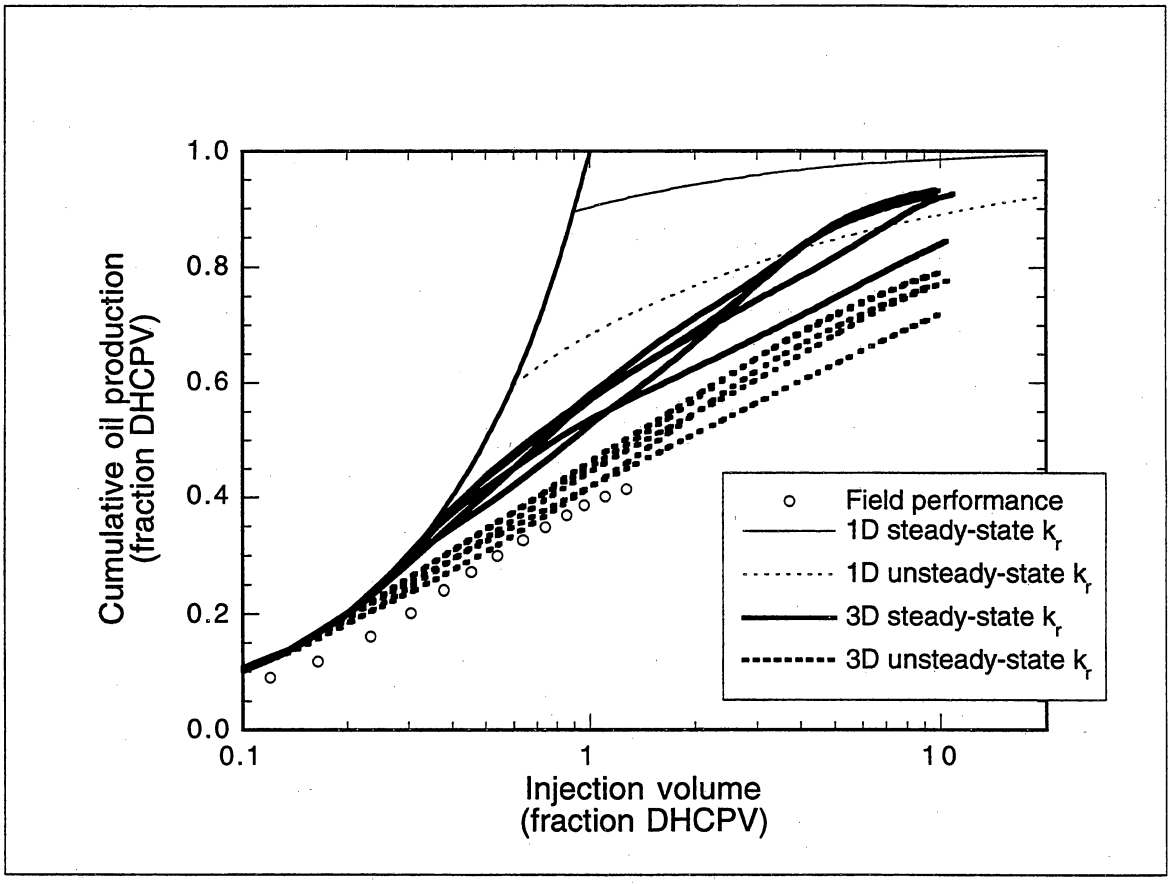

Figure 33. Field performance in sections 5–8, one-dimensional Buckley-Leverett predictions, and three-dimensional waterflood simulations using partially completed wells. Each set of five simulations compares different realizations of the layer-average stochastic model. The k_v/k_h ratio was 0.01; the average s_{oi}-s_{or} model was used to convert field data to DHCPV.

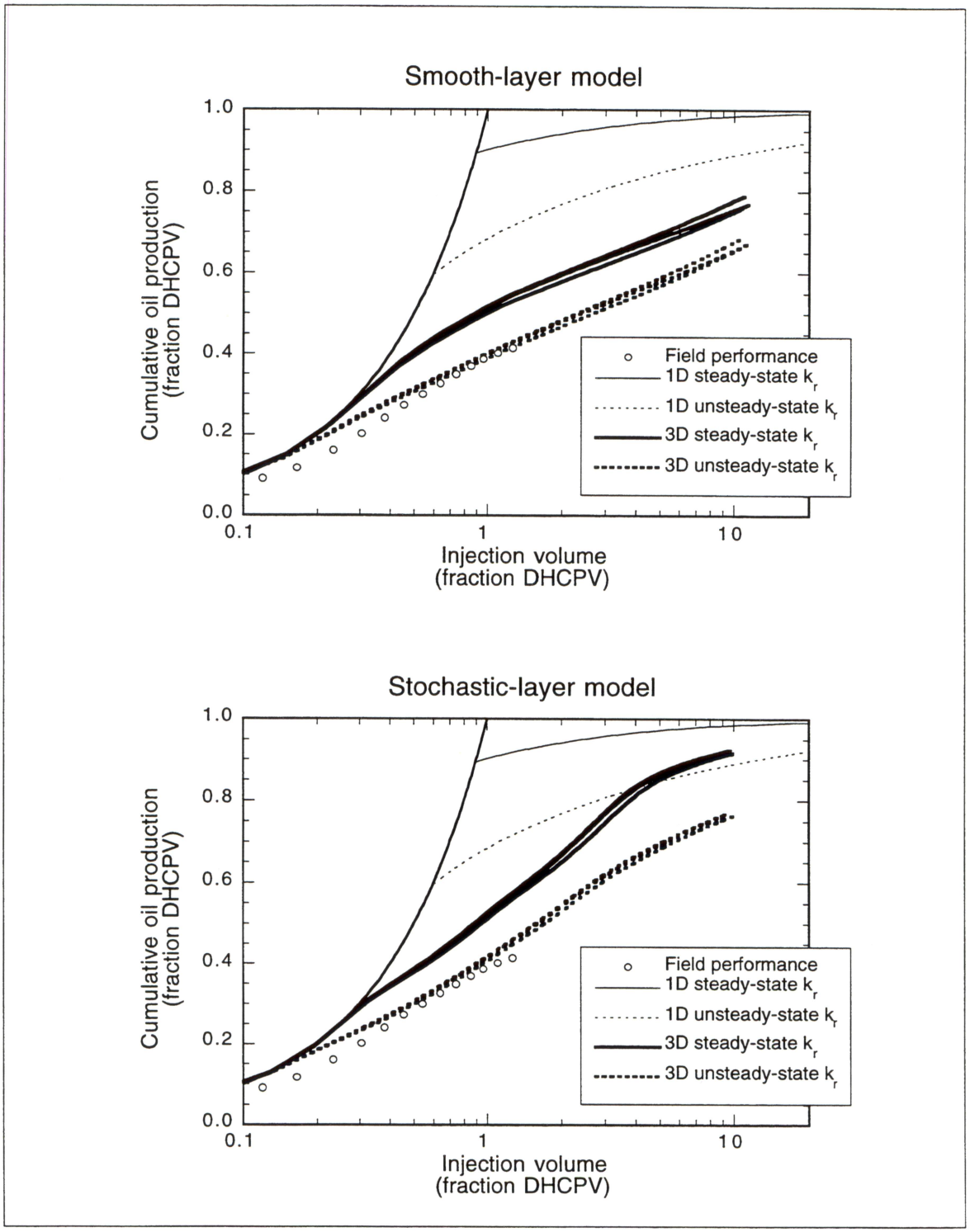

Figure 34. Field performance in sections 5–8, one-dimensional Buckley-Leverett predictions, and three-dimensional waterflood simulations using the smooth-layer model and one realization of the stochastic-layer model. Each set of three simulations compares (a) separately generated ϕ, k, and s_{wi}, (b) k and s_{wi} computed with log models from ϕ, and (c) ϕ and s_{wi} computed with log models from k. The k_v/k_h ratio was 0.01, the average s_{oi}-s_{or} model was used to convert field data to DHCPV, and the wells were partially completed.

Injectivity predictions

Without pressure-transient data, it is impossible to establish the wellbore-model parameters in the waterflood simulations. Thus, predicted and field injectivities cannot be compared unambiguously; the predictions depend on the effective wellbore radius and skin factor as well as the grid-block flow properties. Nevertheless, it is possible to draw some conclusions regarding the effect of several model parameters on injectivity prediction.

First of all, the predicted injectivities were all too low, regardless of the heterogeneity or relative permeability models (table 2). The highest injectivity, 0.0019 DHCPV/well-year in the direct-stochastic model with unsteady-state relative permeabilities, is about a factor of three smaller than the average injectivity observed in the field. Factors that may combine to account for the low injectivity predictions include (1) unknown wellbore-model parameters, particularly the skin factor, which should probably be negative to account for hydraulic fractures, (2) errors in prediction of permeability from well logs,

	Steady-state k_r Injectivity $\left(\frac{\text{640 acre DHCPV}}{\text{well year}}\right)$	Unsteady-state k_r Injectivity $\left(\frac{\text{640 acre DHCPV}}{\text{well year}}\right)$
Uniform	0.00029	0.00045
Constant-layer	0.00035	0.00055
Stochastic-layer	0.00055	0.00085
Smooth-layer	0.00099	0.00153
Direct-stochastic	0.00121	0.00188

Table 2. Predicted injectivities from waterflood simulations with partially completed wells and a k_v/k_h ratio of 0.01. The injectivity listed for the stochastic-layer heterogeneity model is the average from five realizations. The different heterogeneity models are sorted in order of increasing predicted injectivity.

k_v/k_h Ratio	Steady-state k_r Injectivity	Unsteady-state k_r Injectivity
(dimensionless)	$\left(\frac{\text{640 acre DHCPV}}{\text{well year}}\right)$	$\left(\frac{\text{640 acre DHCPV}}{\text{well year}}\right)$
1	0.00197	0.00307
0.1	0.00151	0.00236
0.01	0.00121	0.00188
0.001	0.00094	0.00145

Table 3. Predicted injectivities from waterflood simulations with partially completed wells and the direct three-dimensional stochastic heterogeneity model.

(3) scaleup inaccuracies, particularly in the core-to-log scale, and (4) natural fractures.

The unsteady-state relative permeability model always produced higher injectivities, all other things being equal. This effect is expected from the higher water relative permeabilities in the unsteady-state model and is consistent with the lower predicted waterflood recoveries; higher water mobilities are usually associated with less efficient oil displacement.

The uniform model had the lowest injectivities, in part because it cannot account for the generally higher permeabilities in the top half of the formation where the wells are completed. The injectivities increased through the other heterogeneity models in exactly the same order as decreasing waterflood recovery. Again, higher water mobilities are associated with lower waterflood recoveries; the models with more pathways for channeling of water produced both higher injectivities and more bypassing of oil.

The predicted injectivity was also dependent on the k_v/k_h ratio (table 3). Higher vertical permeabilities produced higher injectivities; they also produced higher oil recoveries due to more effective sweep of the bottom half of the formation. Notice that with variation of vertical permeability the

association between injectivity and oil recovery is *opposite* that observed with different heterogeneity or relative-permeability models. When vertical permeability was changed, the injectivity and oil recovery increased or decreased together; when the heterogeneity or relative-permeability models were changed, the injectivity and oil recovery moved in opposite directions. Thus, with adequate pressure-transient data to determine effective wellbore parameters, it might have been possible to distinguish the effects of vertical permeability and relative permeability by simultaneous comparison with injectivity and waterflood-displacement observations.

Incremental recovery from well recompletions

Well completions are the only parameters explored in this study that affect South Cowden waterflood oil recovery and are under direct control by field operators. Thus, it was useful to estimate the additional oil that might be recovered by recompleting the wells to better sweep the bottom half of the formation. This was easily accomplished by running an additional simulation with wells recompleted at a time corresponding approximately to the current waterflood maturity (fig. 35). The direct three-dimensional stochastic-heterogeneity model was used with the unsteady-state relative permeabilities and a k_v/k_h ratio of 0.01 because that combination resulted in the largest possible injectivity while achieving a reasonable match to the observed waterflood oil displacement. Incremental recovery was computed by subtracting the base case with partial completions from the recompletion case.

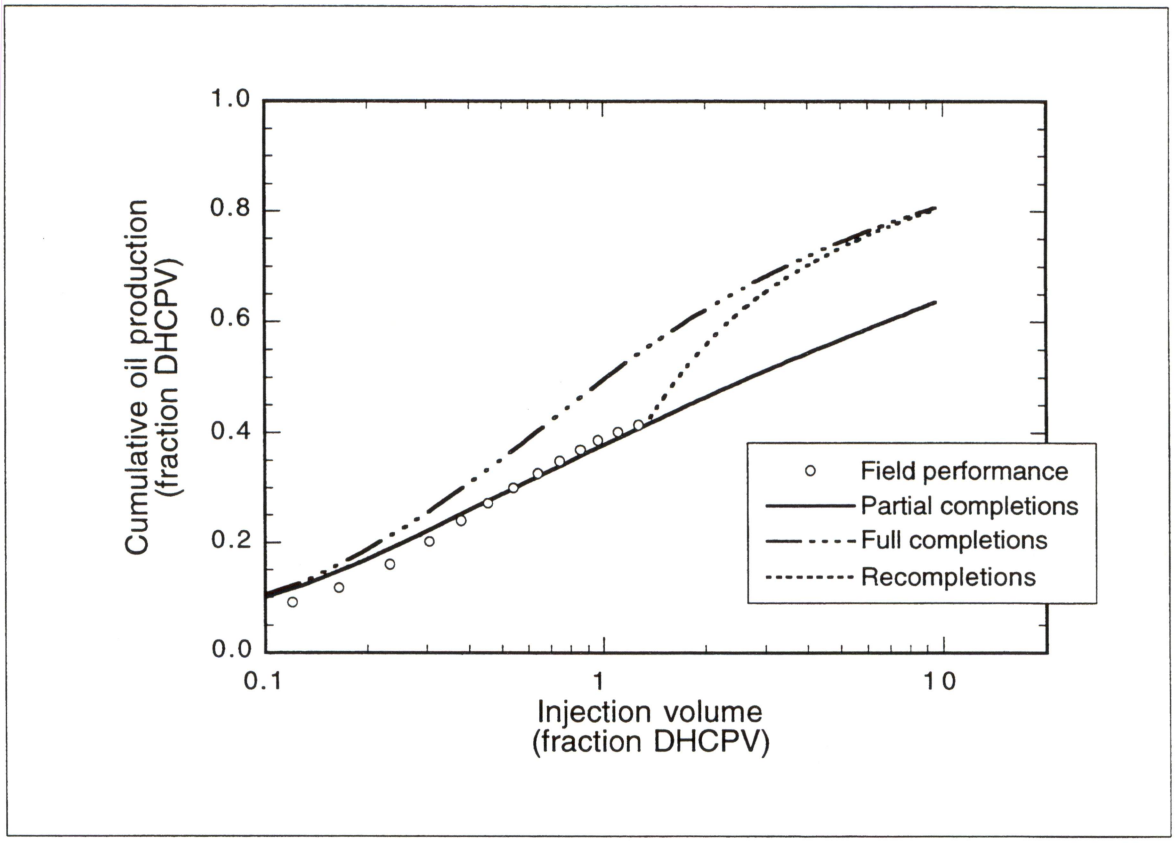

Figure 35. Field performance and three-dimensional waterflood simulations using the direct three-dimensional stochastic-heterogeneity model and the unsteady-state k_r model. The k_v/k_h ratio was 0.01, and the average s_{oi}-s_{or} model was used to convert field data to DHCPV.

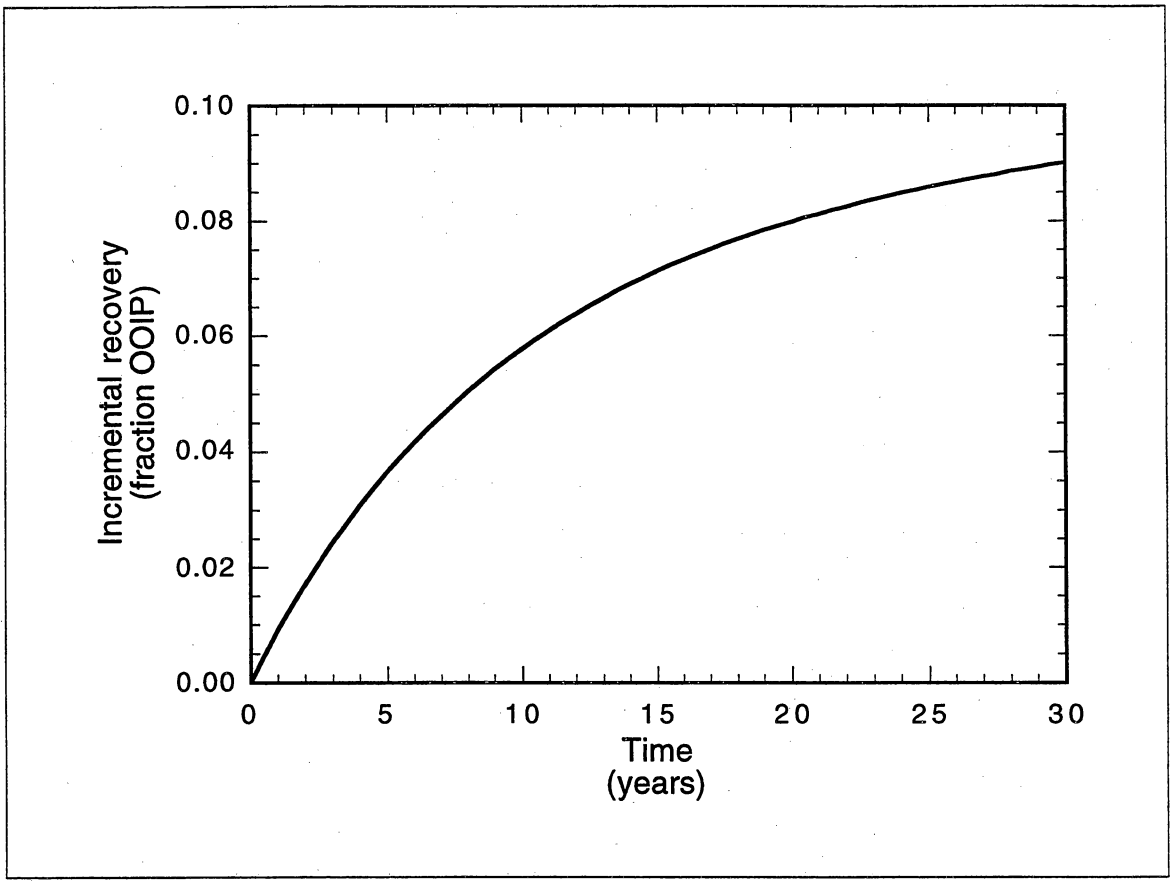

Figure 36. Estimated incremental oil recovery in the South Cowden field from recompletion of wells to sweep the bottom half of the formation. Time zero is the time of recompletion, approximately one DHCPV injection.

The model in its original form underpredicted injectivity by about a factor of three, making the time scale of the incremental-recovery estimate incorrect. Fortunately, gravity effects are unimportant in the South Cowden waterflood, and injection rate has little effect on waterflood-displacement predictions expressed on a DHCPV basis. Thus, the injection rate affects *only* the time scale of the prediction, which can be corrected by simply rescaling it to match the observed injectivity (fig. 36). In ten years the estimated additional recovery will be about 6 percent of the original oil in place if the wells are recompleted now. The prediction applies to portions of sections 5–8 completely above the water-oil contact with a current well completion strategy that sweeps only the top half of the formation. In section 6, for example, the incremental recovery in ten years is estimated at 2 million barrels.

Conclusions and Recommendations

Completion of injectors and producers in only the top portion of the South Cowden reservoir is partly responsible for the historically poor waterflood performance. The effect on oil recovery is most pronounced in areas of the field where the formation is completely above the water-oil contact and the wells are completed only in the top half. Recompletion of the wells through the entire formation is predicted to improve recovery in ten years by 6 percent of the original oil in place in those areas of the field.

The direct-stochastic model produced the best fit to waterflood performance and injectivity, but the simpler smooth-layer model was almost as good. The model based on stochastic-layer averages was less accurate. The constant-layer and uniform models were the least accurate, as expected. These results reaffirm the importance of heterogeneities at the scale of the grid blocks used in the study. However, there is only a slight advantage for stochastic modeling at this scale when high-frequency cycle correlations and property interpolations are informed by closely spaced well data, as in South Cowden.

Some departure from either the whole-core scale k_v/k_h or core-plug scale steady-state relative permeabilities was required for a reasonable match of waterflood displacement. Otherwise, the predicted recovery is too high. Comparison of the observed and predicted injectivities suggests that the behavior should not be modeled with reduced k_v/k_h alone. The best representation of reality probably involves some combination with effective relative permeability.

The difficulty in matching field performance with the steady-state k_r model suggests that heterogeneities smaller than the grid blocks are important to waterflood performance in the South Cowden reservoir. An effective k_r to properly account for these heterogeneities should be less favorable than the steady-state k_r measured on core plugs. By coincidence, the unsteady-state k_r model is unfavorable enough to give a reasonable history match. However, routine use of unsteady-state k_r's to approximate effective k_r's is not

recommended; they are a result of different heterogeneity scales. Further research is recommended on the effects of fine-scale heterogeneity and k_r scaleup in carbonate reservoirs.

Vertical flow restriction is important in the South Cowden reservoir because of the partially completed wells; it inhibits sweep in the lower part of the formation. The effect was modeled conveniently with a constant reduced k_v/k_h ratio, but the restrictions may be caused by thin barriers to vertical flow not explicitly accounted for in any of the heterogeneity models. Further research is recommended on the characterization and modeling of vertical flow barriers in carbonate reservoirs.

The predicted injectivities were consistently too low. The best model under-predicts injectivity by a factor of three, but uncertainties in wellbore-model parameters and permeability prediction from well logs may account for most of the discrepancy. Single-phase permeability scaleup from small-scale heterogeneities may account for the rest. Natural fractures may also play a role.

An attempt was made in several models to test the effect of imperfect correlation between porosity, permeability, and initial water saturation. No significant effect was observed. However, core-scale correlations between these properties are much lower than in the models, and noise in the initial-residual model was not tested at all. These effects have not been adequately explored; additional research is recommended.

Acknowledgments

The author is grateful to Jerry Lucia and Larry Lake for helpful advice during the course of this study. Steve Ruppel and Roger Barnaby provided insight into Grayburg geology in both subsurface and outcrop. Andy Czebieniak manipulated well-log and core data, and produced the smooth interpolated maps. Joseph Yeh performed the volumetric calculations. Fred Wang was helpful in the early stages of the project, particularly with the production database.

Funding for this project was provided by the industrial associates of the Reservoir Characterization Research Laboratory for Carbonate Studies and by DOE contract DE-AC22-93BC14895. Geomath, Inc. provided the Isatis geostatistical analysis software package used for parts of this study.

References

Amyx, J.W., Bass, D.M., and Whiting, R.L., 1960, *Petroleum Reservoir Engineering*: New York, McGraw-Hill, 610 p.

Barnaby, R.J., and Ward, W.B., 1995, Sequence stratigraphic framework, high-frequency cyclicity, and three-dimensional heterogeneity: Grayburg Formation, Brokeoff Mountains, New Mexico, *in* Pause, P.H., and Candelaria, M.P., eds., *Carbonate Facies and Sequence Stratigraphy: Practical Applications of Carbonate Models*: PBS-SEPM Publication 95-36 and PBGC Publication 5-95, 37–49.

Collins, R.E., 1990, *Flow of Fluids Through Porous Materials*: Englewood Colorado, Research & Engineering Consultants, 270 p.

Craft, B.C, Hawkins, M.F., and Terry, R.E., 1991, *Applied Petroleum Reservoir Engineering* (2nd ed.): Englewood Cliffs New Jersey, Prentice-Hall, 431 p.

Deutsch, C.V. and Journel, A.G., 1992, *GSLIB—Geostatistical Software Library and User's Guide*, New York, Oxford University Press, 340 p.

Grant, C.W., Goggin, D.J., and Harris, P.M., 1994, Outcrop analog for cyclic-shelf reservoirs, San Andres formation of Permian Basin: stratigraphic framework, permeability distribution, geostatistics, and fluid-flow modeling: *AAPG Bulletin*, **78** (1), 23–54.

Gupta, A.D., Pope, G.A., Sepehrnoori, K., and Thrasher, R.L., 1986, A symmetric, positive definite formulation of a three-dimensional micellar/polymer simulator: *SPE Reservoir Engineering*, 622–632.

Isaaks, E.H., and Srivastava, R.M., 1989, *An introduction to applied geostatistics*: New York, Oxford University Press, 561 p.

Kerans, C., Lucia, F.J., and Senger, R.K., 1994, Integrated characterization of carbonate ramp reservoirs using Permian San Andres Formation outcrop analogs: *AAPG Bulletin*, **78** (2), 181–216.

Kerans, C., and Nance, H.S., 1991, High-frequency cyclicity and regional depositional patterns of the Grayburg Formation, Guadalupe Mountains, New Mexico, *in* Meander-Roberts, S., Candelaria, M.P., and Moore, G.E, eds., *Sequence Stratigraphy, Facies and Reservoir Geometries of the San Andres, Grayburg and Queen Formations, Guadalupe Mountains, New Mexico and Texas*: Permian Basin Section, Society of Economic Paleontologists and Mineralogists Publication 91-32, 53–96.

Liu, J., Delshad, M., Pope, G.A., and Sepehrnoori, K., 1994, Application of higher-order flux-limited methods in compositional simulation: *Transport in Porous Media*, **16** (1), 1–29.

Liu, J., Pope, G.A., and Sepehrnoori, K., 1995, A high-resolution finite-difference scheme for nonuniform grids: *Applied Mathematical Modeling*, **19**, 162–172.

Lucia, F.J., 1995, Rock-fabric/petrophysical classification of carbonate pore space for reservoir characterization: *AAPG Bulletin*, **79** (9), 1275–1300.

Lucia, F.J., 1996, Petrophysical characterization of the South Cowden Grayburg field, Ector County, Texas: in press.

Pope, G.A., and Nelson, R.C., 1978, A chemical flooding compositional simulator: *Society of Petroleum Engineers Journal*, **18**.

Romeu, R.K., and Noetinger, B., 1995, Calculation of internodal transmissivities in finite difference models of flow in heterogeneous porous media: *Water Resources Research*, **31** (4), 943–959.

Ruppel, S.C., and Bebout, D.G., 1996, Effects of stratal architecture and diagenisis on reservoir development in the Grayburg formation: South Cowden field, Ector County, Texas: Fossil Energy, U.S. Department of Energy, annual contract report, DOE/BC/14895-10, 80 p.

Senger, R.K., Lucia, F.J., Kerans, C., and Ferris, M.A., 1991, Dominant control on reservoir-flow behavior in carbonate reservoirs as determined from outcrop studies, *in* Linville, B., Burchfield, T.E, and Wesson, T.C., eds., *Reservoir Characterization III*: Tulsa, Pennwell, 107–150.

Suter, V.E., Jenkins, W.D., Gray, R., and Matchus, E.J., 1961, Engineering report, Moss Unit, South Cowden field, Ector County, Texas: Moss Unit engineering subcommittee, report prepared for the operators of the proposed Moss Unit, 28 p.

Unocal, 1962, Exhibits for hearing on application of the Union Oil Company of California for a unit allowable for the Moss Unit (Grayburg Dolomite), South Cowden field, Ector County, Texas, 11 p.

Wang, F.P., Lucia, F.J., and Kerans, C., 1994, Critical scales, upscaling and modeling of shallow-water carbonate reservoirs: Society of Petroleum Engineers, 1994 SPE Permian Basin Oil and Gas Recovery Conference, Midland, March 16–18, 765–774.

Young, A., and Vaughn, J.C., 1957, Addis-Johnson-Foster-South Cowden field, *in* Herald, F.A., ed., *Occurrence of Oil and Gas in West Texas*: Austin, The University of Texas Publication No. 5716, 17–22.